



Faculteit Bio-ingenieurswetenschappen

Academiejaar 2015-2016

## **Spatio-temporal modelling of filter cake formation in filtration processes**

**Bram De Jaegher**

Promotor: Prof. dr. ir. Ingmar Nopens & dr. ir. Jan Baetens

Tutor: ir. Wouter Naessens

Masterproef voorgedragen tot het behalen van de graad van  
Master in de bio-ingenieurswetenschappen: Chemie en bioprocestechnologie

De auteur en promotor geven de toelating deze scriptie voor consultatie beschikbaar te stellen en delen ervan te kopiëren voor persoonlijk gebruik. Elk ander gebruik valt onder de beperkingen van het auteursrecht, in het bijzonder met betrekking tot de verplichting uitdrukkelijk de bron te vermelden bij het aanhalen van resultaten uit deze scriptie.

The author and promoter give the permission to use this thesis for consultation and to copy parts of it for personal use. Every other use is subject to the copyright laws, more specifically the source must be extensively specified when using results from this thesis.

Ghent, June 3, 2016

The promoters,

Prof. dr. ir. Ingmar Nopens

dr. ir. Jan Baetens

The tutor,

The author,

ir. Wouter Naessens

Bram De Jaegher

# Acknowledgement

It all started with a bright summer's day in August when I timidly entered the simulation lab of the notorious department of Mathematical Modelling, Statistics and Bioinformatics. Now, ten months later, I can proudly present this master thesis. Despite the vast amount of work and the various complaints of my computer, I can confidently say that I consider this year as a very positive and enriching period of my student career. However, the result of this master dissertation would not have been the same without a few people and therefore I would like to pay them my respects.

First of all, thank you Ingmar Nopens and Jan Baetens for your supervision and thorough corrections. Second of all, I would like to thank Wouter Naessens for being an awesome supervisor and providing guidance throughout this thesis. I am truly sorry for the hour-long, brain frying discussions on the force balance and the heavy workload I put on your shoulders during the first and last weeks. Michael Ghijs, for showing me the relativity of deadlines and the relevance of the Beatles in data storage. May the lift force be with you!

On a more serious note, thank you Timothy Van Daele for helping me with all my OpenFOAM, LaTeX and Github questions and good luck with the finalisation of your PhD. Stijn Van Hoey, for aiding me with the MATLAB, Github and Linux related questions. Next, a special notification for my fellow simulation lab thesis friends; Arthur, Laurentijn, Sofie, Annelies and Bavo for the occasional lighthearted chat and all members BIOMATH and KERMIT for the friendly and welcoming environment. Muchas gracias José por los dátiles.

On a more personal note, a special thanks to my girlfriend, Nancy, for the corrections, support and for being an amazing person. My parents, for all their unconditional support. Finally, I would like to thank "*Wa boel é da ier?*" for all the great experiences during these five years at 't Boerekot and I wish you all the best of luck.



# Summary

At present time, membrane filtration processes suffer from a high operational cost due to fouling abatement measures. The description of fouling mechanisms is still highly empirical and does not provide an adequate framework for the development of decision support tools to aid a cost-effective operation of these processes. The objective of this master dissertation is the development and evaluation of a spatio-temporal model to describe particle behaviour in a realistic and accurate manner in order to unravel the mechanisms of filter cake formation. This model aims to pinpoint the most influential processes that should be included in the next generation of decision support tools for filtration processes.

In the context of this dissertation, a literature review was performed to identify the current fouling modelling approaches and to provide a overview of the available profilometric techniques for the calibration and validation of the model under development. The filter cake formation model of Ghijs (2014) was further extended to a three-dimensional model, the representation of the feed flow was extended to multidisperse suspensions, a new and highly efficient collision detection algorithm was implemented and a user-friendly graphical user interface was developed for the analysis of the simulation results.

A laboratory scale microfiltration device was designed with computational fluid dynamics for the calibration/validation of the model and a qualitative validation, based on the Segré-Silberberg effect, was performed. The latter indicated some imperfections in the force balance on the flowing particles. A scenario analysis was carried out to assess the behaviour of the model under various operational conditions.

The simulations and qualitative validation led to a clear understanding of some of the modelling deficits and shortcomings, such as the formation of narrow filter cake patches and the absence of appropriate wall repulsion effects. Still, with an eye on the future development of the model, guidelines are provided to resolve these issues.

In the end, it can be concluded that a lot of progression was made towards a realistic representation of filter cake formation processes. Furthermore, a lot of knowledge was gained concerning their underlying mechanisms which was, after all, the main objective of this master thesis.



# Samenvatting

Momenteel hebben membraanfiltratieprocessen een grote operationele kost die vooral te wijten is aan de genomen maatregelen tegen de vervuiling van het membraan. De beschrijving van deze vervuylingsmechanismen is nog steeds zeer empirisch en biedt geen goed kader voor de ontwikkeling van beslissingsondersteunende systemen. Deze systemen kunnen onder andere de kosteneffectiviteit van deze processen verbeteren. Het doel van deze thesis is de ontwikkeling en evaluatie van een spatio-temporeel model dat het gedrag van gesuspendeerde partikels in een filtratiesysteem op een realistische en accurate manier kan beschrijven. Dit model kan waardevolle inzichten leveren in de belangrijkste onderliggende mechanismen van filterkoekvorming. Deze mechanismen kunnen dan opgenomen worden in de volgende generatie aan beslissingsondersteunende systemen.

In het kader van dit proefschrift werd een literatuuronderzoek uitgevoerd dat een overzicht biedt van de huidige membraanvervuilingsmodellen. Tevens wordt een overzicht gegeven van de beschikbare profilometrische technieken voor de kalibratie en validatie van het model in ontwikkeling. Het spatio-temporeel model van Ghijss (2014), dat de filterkoekvorming beschrijft in membraanbioreactoren, werd verder uitgebouwd naar een driedimensionaal model. Een polydisperse voorstelling van de disperse fase werd bewerkstelligd en een nieuw en efficiënt collisiedetectie-algoritme werd geïmplementeerd. Voor de analyse van de simulatieresultaten werd een gebruiksvriendelijke grafische gebruiksomgeving ontwikkeld.

Een microfiltratie pilootopstelling werd ontwikkeld via numerieke stromingsleer voor de kalibratie/validatie van het model en een kwalitatieve validatie werd uitgevoerd op basis van het Segré-Silberberg effect. Dit laatste toonde een aantal onvolmaaktheden aan in de krachtenbalans over de gesuspendeerde partikels. Vervolgens werd een scenarioanalyse uitgevoerd om het gedrag van het model onder verschillende operationele condities te evalueren.

De simulatieresultaten en kwalitatieve validatie hebben geleid tot een duidelijk inzicht in enkele tekortkomingen van het model zoals de vorming van kleine filterkoektorens en de afwezigheid van de gepaste wandrepulsie-effecten. Met het oog op de toekomstige ontwikkeling van het model werden een aantal richtlijnen verschafft om deze kwesties aan te pakken. Er kan besloten worden dat er veel vooruitgang geboekt is naar een realistische voorstelling van filterkoekvormende processen, waarbij veel inzicht verworven is in de onderliggende mechanismen; het uiteindelijke hoofddoel van deze dissertatie.



# Contents

<b>Acknowledgement</b>	i
<b>Summary</b>	iii
<b>Samenvatting</b>	v
<b>Contents</b>	viii
<b>List of Symbols</b>	ix
<b>List of Abbreviations</b>	xiii
<b>1 Introduction</b>	1
1.1 Introduction . . . . .	1
1.2 Problem statement . . . . .	2
1.3 Objectives of this research . . . . .	3
1.4 Outline: the roadmap through this dissertation . . . . .	3
<b>2 Literature Review</b>	5
2.1 Membrane fouling . . . . .	5
2.2 Membrane fouling models . . . . .	6
2.2.1 Resistance-in-series models . . . . .	7
2.2.2 Advanced mechanistic models . . . . .	8
2.2.3 Data-driven models . . . . .	19
2.3 Profilometry . . . . .	22
2.3.1 Non-optical methods . . . . .	22
2.3.2 Optical methods . . . . .	23
<b>3 Spatio-temporal model of filter cake formation</b>	27
3.1 Assumptions . . . . .	28
3.2 Dispersed phase . . . . .	29
3.3 Filter cake formation . . . . .	31
3.4 Continuous phase . . . . .	31

3.4.1	Fluid dynamics . . . . .	31
3.4.2	Computational fluid dynamics . . . . .	33
<b>4</b>	<b>Model development</b>	<b>35</b>
4.1	Polydispersity . . . . .	35
4.1.1	Particle sampling . . . . .	36
4.1.2	Filter cake formation . . . . .	38
4.2	Extension to a three-dimensional model . . . . .	40
4.3	Parallelisation . . . . .	41
4.4	Model architecture . . . . .	41
4.5	Software . . . . .	43
4.5.1	MATLAB . . . . .	43
4.5.2	Python . . . . .	43
4.5.3	SALOME . . . . .	44
4.5.4	OpenFOAM . . . . .	44
4.6	Post-processing user interface . . . . .	44
<b>5</b>	<b>Results and discussion</b>	<b>47</b>
5.1	Calibration and validation: model-based design of a filtration unit . . . . .	47
5.2	Case studies . . . . .	52
5.2.1	Setup . . . . .	52
5.2.2	Mesh independence of the continuous phase . . . . .	55
5.2.3	The Segré-Silberberg effect: a qualitative validation . . . . .	57
5.2.4	Mesh independency of the agent-based model . . . . .	61
5.2.5	Spatial segregation of the suspended particles . . . . .	61
5.2.6	Effect of polydispersity . . . . .	63
<b>6</b>	<b>General discussion and perspectives</b>	<b>65</b>
6.1	Remarks on the bulk phase force balance . . . . .	65
6.2	Filter cake formation . . . . .	66
6.3	Coupling ABM and continuous model . . . . .	67
6.4	Sources of numerical instability . . . . .	69
6.5	Profilometry . . . . .	69
<b>7</b>	<b>Conclusion</b>	<b>71</b>
<b>Bibliography</b>		<b>73</b>
<b>A Appendix: Technical drawing microfilter</b>		<b>81</b>

# List of Symbols

Symbol	Description	Unit
$A$	inlet area	[m <sup>2</sup> ]
$A_m$	membrane area	[m <sup>2</sup> ]
$\alpha$	specific filtration resistance	[m kg <sup>-1</sup> ]
$c_b$	bulk concentration	[kg m <sup>-3</sup> ]
$c_c^b$	bulk concentration of particles that are retained on the membrane surface	[kg m <sup>-3</sup> ]
$c_m^b$	the mass concentration of particles able to penetrate the membrane	[kg m <sup>-3</sup> ]
$c_c$	mass concentration of the cake layer	[kg m <sup>-3</sup> ]
$c_m$	concentration on membrane surface	[kg m <sup>-3</sup> ]
$D_h$	hydraulic diameter	[m]
$d_p$	particle diameter	[m]
$\bar{d}_p$	mean diameter of bulk particles	[m]
$\Delta i$	thickness of a filter cake slice	[m]
$\Delta p$	pressure drop	[Pa]
$\Delta p_c$	pressure drop over cake layer	[Pa]
$\Delta p_{t,\text{eff}}$	the effective transmembrane pressure acting on the membrane surface	[Pa]
$\Delta t$	time step	[s]
$E$	probability of deposition	[ - ]
$\epsilon$	actual filter cake porosity	[ - ]
$\epsilon_m$	membrane porosity	[ - ]
$\epsilon_{\text{sph}}$	filter cake porosity for perfect spheres	[ - ]

Symbol	Description	Unit
$\vec{F}_{\text{am}}$	added mass force	[N]
$\vec{F}_{\text{arch}}$	Archimedes force	[N]
$\vec{F}_{\text{body}}$	body forces	[N]
$\vec{F}_{\text{drag}}$	drag force	[N]
$\vec{F}_g$	gravitational force	[N]
$\vec{F}_{\text{hist}}$	history force	[N]
$\vec{F}_{\text{hydr}}$	resulting hydrodynamic force	[N]
$\vec{F}_{\text{lift}}$	lift force	[N]
$\vec{F}_p$	pressure gradient induced force	[N]
$\vec{F}_{\text{surf}}$	surface forces	[N]
$F_A$	adhesion force	[N]
$F_d$	drag force	[N]
$F_g$	gravity force	[N]
$F_i$	interparticle force	[N]
$F_l$	lift force	[N]
$F_N$	normal force	[N]
$F_{\text{num}}$	particle size distribution	[-]
$F_t$	tangential shear stress	[N]
$F_\tau$	friction force	[N]
$f$	external body forces	[N m <sup>-1</sup> ]
$f_c$	friction factor	[-]
$g_b$	particle size distribution of the bulk particles	[-]
$g_{\text{cake}}$	particle size distribution of the particles retained by the membrane	[-]
$g_m$	particle size distribution of the particles able to enter the pores	[-]
$J$	flux	[m <sup>3</sup> m <sup>-2</sup> s <sup>-1</sup> ]
$K$	Kozeny constant	[-]
$K_c$	specific cake resistance	[m <sup>-2</sup> ]
$K_d$	rate coefficient of sludge detachment	[s <sup>-1</sup> ]
$K_p$	membrane specific constant	[m <sup>-1</sup> ]
$\kappa$	fluid velocity gradient	[ s <sup>-1</sup> ]
$k$	adhesion parameter	[ s m <sup>-1</sup> ]
$k_c$	model parameter cake layer	[m <sup>2</sup> kg <sup>-1</sup> ]
$k_f$	model parameter fouling	[-]

Symbol	Description	Unit
$k_p$	mass transfer coefficient	$\text{m}^3 \text{ m}^{-2} \text{ s}^{-1}$
$L$	characteristic length	[m]
$l$	cake thickness	[m]
$M$	mass per membrane surface area	$\text{kg m}^{-2}$
$M_{sf}$	mass of sludge in the filter cake	$\text{kg m}^{-2}$
$\mu_f$	fluid dynamic viscosity	$\text{kg m}^{-1} \text{ s}^{-1}$
$\mu_{\max}$	maximum friction	[ - ]
$m$	mass	[kg]
$m_p$	particle mass	[kg]
$m_{\text{tot}}$	total mass inflow of suspended solids during the entire simulation	[kg]
$N$	number of free pores	[ - ]
$N_0$	initial number of membrane pores	[ - ]
$\nu_f$	fluid kinematic viscosity	$\text{m}^2 \text{ s}^{-1}$
$\nabla p$	pressure gradient	$\text{Pa m}^{-1}$
$\Omega$	volume of fluid element	$\text{m}^3$
$\omega$	fraction of retained particles that attach to the cake layer	[ - ]
$P(\mathbf{U}_p)$	adhesion probability	[ - ]
$p_f$	total fraction of depositable particles	[ - ]
$\phi_s$	shape factor	[ - ]
$\psi$	relative kinematic pressure	$\text{m}^2 \text{ s}^{-2}$
$R$	membrane resistance	$\text{m}^{-1}$
$R_b$	pore blocking resistance	$\text{m}^{-1}$
$R_c$	filter cake resistance	$\text{m}^{-1}$
$R_f$	pore blocking and inner membrane fouling resistance	$\text{m}^{-1}$
$R_m$	clean membrane resistance	$\text{m}^{-1}$
$R_t$	total hydraulic resistance	$\text{m}^{-1}$
$Re$	Reynolds number	[ - ]
$Re_p$	particle Reynolds number	[ - ]
$R_{\text{pore}}$	retained weight fraction distribution of the membrane pore size distribution	[ - ]
$\rho_f$	density of the continuous phase	$\text{kg m}^{-3}$

Symbol	Description	Unit
$\rho_{p,m}$	the density of particles in the membrane pores	[kg m <sup>-3</sup> ]
$\rho_s$	density of the bulk particles	[kg m <sup>-3</sup> ]
$S$	specific surface area	[m <sup>2</sup> ]
$S_f$	model parameter fouling saturation	[ - ]
$S_i$	specific surface area of the particles	[m <sup>2</sup> ]
$t$	time	[s]
$t_f$	filtration time/cycle	[s]
$t_{\text{tot}}$	total simulation time	[s]
$\tau$	viscous stress tensor	[N]
$\tau_W$	shear stress	[Pa]
$\theta$	angle of friction	[ - ]
$\theta_c$	critical friction angle	[ - ]
$\mathbf{U}_c$	fluid velocity	[m s <sup>-1</sup> ]
$\mathbf{U}_{cf}$	cross-flow velocity	[m s <sup>-1</sup> ]
$\mathbf{U}_m$	maximum channel velocity	[m s <sup>-1</sup> ]
$\mathbf{U}_p$	particle velocity	[m s <sup>-1</sup> ]
$\mathbf{U}_r$	relative particle velocity	[m s <sup>-1</sup> ]
$\mathbf{U}_{r,\text{eff}}$	Faxén corrected relative velocity	[m s <sup>-1</sup> ]
$V_p$	particle volume	[m <sup>3</sup> ]
$V_m$	total membrane volume	[m <sup>3</sup> ]
$V_{p,m}$	volume of particles that sediment each filtration cycle	[m <sup>3</sup> ]
$v$	velocity	[m s <sup>-1</sup> ]
$v_d$	diffusion velocity	[m s <sup>-1</sup> ]
$v_g$	gravitational sedimentation velocity	[m s <sup>-1</sup> ]
$v_i$	particle interaction velocity	[m s <sup>-1</sup> ]
$v_l$	inertia lifting velocity	[m s <sup>-1</sup> ]
$v_s$	shear induced diffusion velocity	[m s <sup>-1</sup> ]
$v_{\text{tot}}$	total backtransport velocity	[m s <sup>-1</sup> ]

# List of Abbreviations

ABM	agent-based model
AFM	atomic force microscopy
API	application programming interface
CAD	computer-aided design
CDF	cumulative distribution function
CFD	computational fluid dynamics
CLSM	confocal laser scanning microscopy
DHM	digital holographic microscopy
DICM	differential interference contrast microscopy
DLVO	Derjaguin, Landau, Verwey and Overbeek
FEM	finite element method
FP	Fourier profilometry
FPP	fringe projection profilometry
FVM	finite volume method
GUI	graphical user interface
MBR	membrane bioreactor
MP	Moiré profilometry
OCT	optical coherence tomography
PDE	partial differential equation

PMF	probability mass function
PSD	particle size distribution
RIS	resistance-in-series
SCR	simulation time to computational time ratio
SEM	scanning electron microscopy
SP	stylus profilometry
SS	suspended solids
STM	scanning tunneling microscopy
TMP	transmembrane pressure
WLAC	white light axial chromatism
WLI	white light interferometry

# CHAPTER 1

## Problem statement, research objectives

### 1.1 Introduction

Membrane filtration is a purely physical separation process where a suspension is drawn through a semi-permeable membrane and the suspended constituents larger than the membrane pores are retained. In descending pore size, a distinction is made between microfiltration, ultrafiltration, nanofiltration and reverse osmosis. Figure 1.1 gives an overview of the different membrane filtration types along with the class of solids that are typically retained by the membrane.

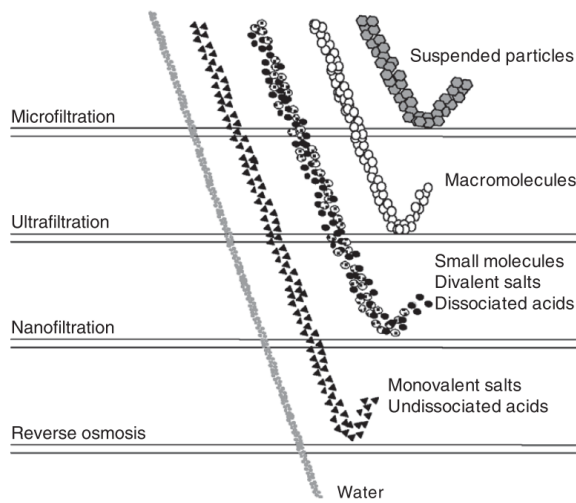


**Figure 1.1:** An overview of the different membrane filtration types (Luque et al., 2008).

The presence of membrane filtration in wastewater treatment processes is well established by its main application, the membrane bioreactor (MBR). An MBR is a combination of a biological reactor for the conversion of solutes to suspended solids (activated sludge) combined

with a membrane filter to remove these solids and thereby produce clean water (Judd, 2011). Membrane filtration replaces the traditional, gravitational sedimentation of activated sludge and produces water with a significantly higher quality (Judd, 2008). Moreover, MBRs are more robust and are able to handle higher concentrations of suspended solid, leading to a higher loading capacity and consequently more compact treatment plants. Other, more exotic, applications of membrane filtration in wastewater treatment are, among others, the removal of emulsified oils and the recovery of heavy metals (Fu and Wang, 2011; Cheryan and Rajagopalan, 1998).

Nowadays, membrane filtration is also being employed in a vast range of industrial, medical and biotechnological processes and the market of membrane filtration is ever growing (Scott and Highes, 2012; Luque et al., 2008). Important applications of membrane filtration can be found in the paper production industry for lignosulfonate fractionation and color removal (Luque et al., 2008), in the food industry for the clarification of beer, wine and vinegar (Cimini et al., 2013; Ulbricht et al., 2009; Tamime, 2012), in the medical sector for the continuous filtration of blood plasma and in biotechnology for the clarification of fermentation broth (Homsy et al., 2012; Prasad, 2010). Several potential uses for membrane filtration in renewable energy applications, such as biogas upgrading and biodiesel purification, are proposed in literature (Charcosset, 2014; Dubé et al., 2007). In short, membrane filtration has become indispensable in industrial as well as wastewater treatment processes.

There is, nonetheless, a major disadvantage coupled with membrane filtration, i.e. membrane fouling. The continuous feed and retention of suspended solids leads to the formation of fouling layers on top (filter cake) or inside the membrane and increases the resistance towards liquid permeation. Hence, operation of a membrane filtration unit requires continuous fouling control which includes backwashing, aeration and chemical cleaning of the membrane. These procedures are not able to fully regenerate the membrane due to irrecoverable fouling, leading to the insuperable decay of the membrane. The effectuation of fouling control measures and the replacement of membranes gives rise to considerable operational expenses, making membrane filtration a costly technique (Owen et al., 1995).

## 1.2 Problem statement

In spite of the growing importance of membrane filtration in industry and wastewater treatment processes, there is still little understanding of the underlying processes of membrane filtration. In order to suppress fouling and prolong the lifetime of pressure-driven membrane systems as much as possible, the operation is highly conservative. Fouling remediation procedures are performed frequently, leading to a sub-optimal operation which is costly and inefficient both from an energetic and material perspective. Quite some efforts have been put in fouling research, but there is still poor insight in the system dynamics. Efforts to model membrane filtration and the fouling build-up are mostly empirical and typically based on

the resistance-in-series (RIS) approach (Section 2.2.1). Such models are capable of accurately predicting flux decline and transmembrane pressure (TMP) increase over time, but only under the specific operational conditions for which they are calibrated. Hence, they lack extrapolation capacity to accurately predict fouling rates and optimal backflushing frequencies in a general setting. Moreover, RIS models are often overparameterised and require frequent recalibration with a vast amount of data for accurate parameter estimations, making real-time recalibration typically not feasible.

These reasons have led to the fact that efforts have not yet resulted in a universally applicable membrane filtration model, neither do they agree on fundamental fouling principles. An in-depth understanding of the underlying fouling processes will allow for a more responsive, dynamic operation and a better design of filtration installations. Furthermore, the availability of accurate and robust fouling models will enable the implementation of more advanced control strategies, such as internal model control, model-based predictive control, or *in silico* tuning of process controllers.

### 1.3 Objectives of this research

The first objective of this master thesis is the extension of the mechanistic, spatially explicit modelling framework proposed by Ghijs (2014). The model has its limitations and will be critically analysed, extended and polished, so to progress towards a physically more accurate description of all relevant processes contributing to filter cake formation.

The second objective is the model-based design and realisation of a laboratory scale membrane filtration system for the calibration and validation of the abovementioned model.

It should be kept clear at all times that the purpose of this model is not the real-time evaluation of operational conditions, but rather unraveling fouling mechanisms. Hopefully, this model will be able to provide valuable insights into the key mechanisms of membrane fouling needed for the future development of computationally efficient filtration models for dynamic control, backflushing prediction, computer-aided design (CAD), etc.

### 1.4 Outline: the roadmap through this dissertation

This dissertation starts with a literature review of membrane fouling models and profilometric techniques. Chapter 3 provides a description of the model developed by Ghijs (2014). The improvements of this model, performed in this thesis, are discussed in Chapter 4. Next, the results of a qualitative validation of the improved model and a scenario analysis are elucidated in Chapter 5. Chapter 6 addresses the modelling imperfections and provides guidelines for the future development of the model. Finally, this master dissertation presents the conclusions in Chapter 7.



# CHAPTER 2

## Literature Review

In order to further develop and improve the spatio-temporal model of filter cake formation elaborated by Ghijss (2014), it is necessary to thoroughly review the various modelling approaches in literature. In this manner, all processes and accompanying interdependencies can be mapped out, which enables the development of a realistic model comprising all relevant processes. The first part of this chapter is dedicated to this. In the second part of this chapter, a few promising profilometric techniques, necessary for model calibration, will be discussed.

### 2.1 Membrane fouling

Membrane fouling comes in many forms and types. Furthermore, generally accepted membrane fouling terminology is altered by different authors in the field. Before exploring the different models, some important concepts and the associated lexicon will be defined.

Mohammadi et al. (2003) defines membrane fouling as “*[...] the existence and growth of micro-organisms and the irreversible collection of materials on the membrane surface which results in a flux decline.*” However, a more suitable definition is “*[...] the process resulting in loss of performance of a membrane due to deposition of suspended or dissolved substances on its external surfaces, at its pore openings, or within its pores*” by Koros et al. (1996) because it also includes pore fouling.

Depending on the type of membrane filtration (nanofiltration, microfiltration, etc. ), different types of fouling can be encountered during operation. Generally, fouling can be classified as follows:

- scaling: precipitation of substances due to exceeding the solubility product induced by the process of concentration polarisation;
- particulate fouling, inorganic and organic;

- biofouling: fouling effects due to colonisation by bacteria;
- fouling by macromolecular substances;
- chemical reaction of solutes with the membrane polymer and/or its boundary layer;

It is nevertheless important to keep in mind that these are only the main types. It is possible that other, more specific types exist. Some authors prefer to classify fouling in terms of persistency (reversible, irreversible and irrecoverable fouling) whilst others favor a mechanical categorisation (pore blocking, cake formation, intermediate blocking, etc.). Unfortunately, these classifications cannot be compared mutually, as there is no complete parity between any of these types.

Another important phenomenon to elucidate is concentration polarisation. This is the tendency of solutes to accumulate near the membrane. Materials, rejected by the membrane, accumulate in the vicinity of the membrane surface. The thickness of this layer is governed by the hydrodynamics; increasing crossflow velocities and a decreasing membrane flux result in a decreasing thickness. This is partially compensated by diffusion (back diffusion) and under steady-state conditions a balance is established between the forces that transport the solutes to, through and away from the membrane (Judd, 2011).

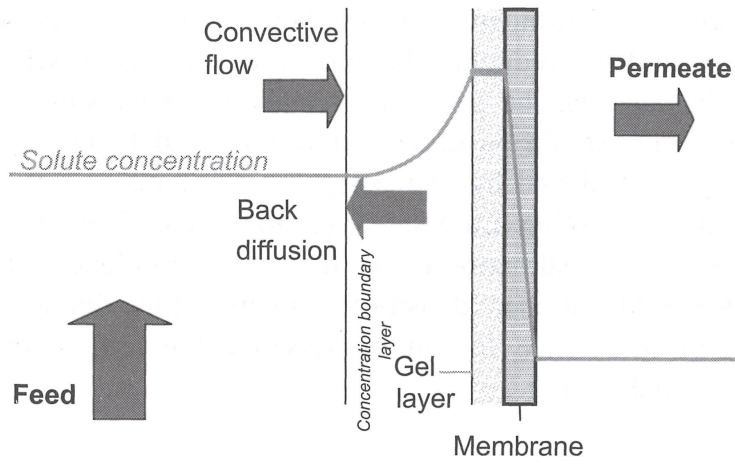


**Figure 2.1:** Schematic representation of the driving forces leading to concentration polarisation in crossflow membrane filtration processes (Judd, 2011).

## 2.2 Membrane fouling models

Now that the lexiconic framework has been established, it is possible to unambiguously describe the different existing modelling approaches that are most relevant for this thesis. Both

mechanistic and data-driven models will be discussed. Here, “data-driven” is regarded as black-box modelling using machine learning techniques, whilst “mechanistic” is regarded as gray-box modelling.

### 2.2.1 Resistance-in-series models

The majority of fouling models are based on the RIS concept. This approach, based on Darcy’s law, Eq. (2.1), defines a membrane resistance  $R$  [ $\text{m}^{-1}$ ] to relate the flux  $J$  [ $\text{m}^3 \text{m}^{-2} \text{s}^{-1}$ ] across the membrane to the TMP or  $\Delta p$  [Pa],

$$\Delta p = J R \mu_f , \quad (2.1)$$

with  $\mu_f$  [ $\text{kg m}^{-1} \text{s}^{-1}$ ] the dynamic viscosity of the fluid.

Typically, the total membrane resistance consists of different resistance terms in series, the clean membrane resistance  $R_m$  [ $\text{m}^{-1}$ ] and various resistances originating from different fouling layers. Mostly they comprise of fouling types from different classifications which is tricky as overlap of the underlying process is possible, e.g. pore blocking and irreversible fouling are not independent. The clean membrane resistance is the inherent resistance of the membrane, which is constant, and is provided by the membrane manufacturer or obtained from pure water filtration experiments (Naessens et al., 2012).

Numerous RIS models are proposed in literature, each introducing different resistance terms. For each resistance term a separate model needs to be developed. These models can be mechanistic, describing the real mechanisms of the process or semi-empirical, requiring more careful calibration (Naessens et al., 2012).

One of the more simple, empirical RIS model is presented in Khan et al. (2009). Here, the total hydraulic resistance  $R_t$  [ $\text{m}^{-1}$ ] is defined as the sum of the cake resistance  $R_c$  [ $\text{m}^{-1}$ ] caused by deposition of particulate matter on top of the membrane, the fouling resistance  $R_f$  [ $\text{m}^{-1}$ ] due to pore blocking and adsorption of matter within the membrane and the abovementioned clean membrane resistance  $R_m$ , i.e.

$$R_t = R_m + R_c + R_f \quad (2.2)$$

The resistance terms in Eq. (2.2) are calibrated with different filtration experiments. Measurements of the TMP and flux in combination with Darcy’s law result in values for the different resistance terms.  $R_m$  is determined through filtration experiments on a chemically cleaned membrane, while  $R_f$  is measured with a membrane where the cake was removed after a previous filtration experiment.  $R_t$  was determined from the final flux and TMP at the end of the filtration experiments. Finally,  $R_c$  can be obtained by re-arranging Eq. (2.2) and filling in the known resistances. This approach is very straightforward, the resistance terms are obtained by directly fitting Eq. (2.1) to the experimental data.

A more elaborate approach is described by Wintgens et al. (2003). The same resistance terms are used as in the previous model, but each term is described by semi-empirical equations instead of deriving them directly from Darcy's law. The cake resistance  $R_c$  is assumed to be dependent on the concentration of the cake layer forming component at the membrane surface  $c_m$  [ $\text{kg m}^{-3}$ ] as follows,

$$R_c = k_c c_m, \quad (2.3)$$

with  $k_c$  [ $\text{m}^2 \text{kg}^{-1}$ ] an empirical parameter.

When considering concentration polarisation effects,  $c_m$  follows from

$$J = k_p \ln \left( \frac{c_m}{c_b} \right), \quad (2.4)$$

with  $k_p$  [ $\text{m}^3 \text{m}^{-2} \text{s}^{-1}$ ] the local mass transfer coefficient and  $c_b$  [ $\text{kg m}^{-3}$ ] the bulk concentration of suspended solids.

The authors assume that the fouling resistance  $R_f$  is dependent on the total permeate volume produced during filtration as

$$R_f = S_f (1 - e^{-k_f \int_0^t J(t) dt}). \quad (2.5)$$

with  $S_f$  [-] a factor that represents the specific surface area of the membrane that can be covered by fouling products and  $k_f$  [-] an empirical parameter.

The model parameters  $k_c$ ,  $S_f$ ,  $k_f$ ,  $k_p$  and the clean membrane resistance  $R_m$  are obtained through calibration.

Model validation shows that this approach is able to accurately predict the flux. It is important to note that validation was done with data from another filtration unit, independent from the calibration dataset. Some of the RIS models, discussed in this section, are capable of closely approximating the impact of fouling on process variables such as flux and TMP. Still, these semi-empirical models do not yield insight into the different fouling mechanics. Our objective is to better characterise the processes and mechanics behind fouling. With this in mind it is necessary to move towards more advanced mechanistic models that aim at fully describing the major physical processes in play. Additionally, such models have the tendency to be more widely applicable, in contrast to the empirical models that need to be recalibrated when applied in other operational conditions.

## 2.2.2 Advanced mechanistic models

As previously mentioned, RIS models dominate the fouling modelling landscape. This section describes the more advanced, mechanistic fouling models. Most of these models also use the RIS approach in which the different resistance terms are described mechanistically. A summary of the basic ideas behind these approaches will be given, followed by a critical review of their strengths and weaknesses.

## Force balance

Lu and Hwang (1993) start from the idea that the cake resistance is largely dependent on the structure of the filter cake and the size of the bulk particles. Consequently, a model is developed that is first of all capable of accurately predicting the cake layer structure in a dead-end, constant pressure filtration system and secondly, incorporates the particle size dependencies.

For a particle that is depositing on the filter cake a critical friction angle is calculated to determine if the particle will “stick” to the surface (membrane or filter cake) or not. This angle of friction  $\theta$  [-] is defined as the angle between the gravity vector and the line between the particle centers, A (depositing particle) and B (deposited particle) (Figure 2.2). Below a certain critical friction angle  $\theta_c$ , the friction between particles A and B is large enough for particle A to deposit on particle B. In contrast, for  $\theta$  values larger than  $\theta_c$ , not enough friction is occurring and particle A will not be able to deposit and slide past particle B.

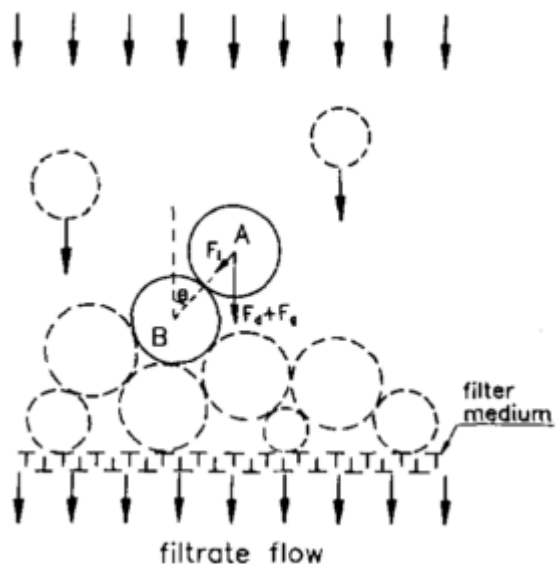


**Figure 2.2:** Representation of the considered forces on a settling particle at the cake surface and the friction angle (Lu and Hwang, 1993).

$\theta_c$  is determined from a force balance on the depositing particle (A). At the critical condition ( $\theta = \theta_c$ ), the tangential forces are in equilibrium with the friction forces, so

$$(F_g + F_d) \sin(\theta_c) = f_c (F_i + (F_g + F_d) \cos(\theta_c)), \quad (2.6)$$

with  $F_i$  [N], the interparticle force,  $F_d$  [N] the drag force,  $F_g$  [N] the gravity force and  $f_c$  [-] the friction factor between particles (Lu and Hwang, 1993). When the values of all forces in Eq. (2.6) are known it is possible to determine  $\theta_c$ . A detailed explanation and derivation

of the different equations for the forces and parameters can be found in the original article by Lu and Hwang (1993). The number of particles arriving at the cake surface is controlled by the concentration and flux. The deposition point is determined by “dropping” particles from a random position onto the cake or membrane and evaluating the angle of friction, as explained above. Hence, a cake structure is obtained for a certain value of  $\theta_c$ . For the particle stacking, perfectly spherical particles are assumed but the porosity can be corrected with a shape factor  $\phi_s$  [-] for other shapes,

$$\phi_s = \frac{1 - \epsilon}{1 - \epsilon_{\text{sph}}}, \quad (2.7)$$

with  $\epsilon$  [-] the actual porosity of the filter cake for non-spherical particles,  $\epsilon_{\text{sph}}$  [-] the porosity of the filter cake determined by the model, assuming perfect spheres. A full mathematical description on the determination of  $\phi_s$  is given in Cross et al. (1985).

Also the process of compression is considered, by calculating a porosity change based on a fluid mass balance. The flux across the filter is calculated with the Kozeny-Carman equation,

$$J = \frac{\Delta p}{l} \frac{\epsilon^3}{\nu_f K S^2 (1 - \epsilon)^2}. \quad (2.8)$$

This relation indicates that the flux  $J$  through a filter with depth  $l$  [m] is influenced by the TMP  $\Delta p$ , the specific surface area  $S$  [ $\text{m}^2$ ], the kinematic viscosity of the fluid  $\nu_f$  [ $\text{m}^2 \text{s}^{-1}$ ], the cake porosity  $\epsilon$  and modulated by the Kozeny constant  $K$  [-].

An expression for the Kozeny constant in function of the porosity is obtained by solving the Navier-Stokes equations and a continuity equation. Which in turn, when combined with Eq. (2.8), gives rise to an equation for the specific filtration resistance  $\alpha$  [ $\text{m kg}^{-1}$ ] of the filter cake (Eq. 2.9).

$$\alpha = K S^2 \frac{1 - \epsilon}{\epsilon^3 \rho_s}, \quad (2.9)$$

where  $\rho_s$  [ $\text{kg m}^{-3}$ ] is the density of the solids.

The predicted average porosity and average specific resistance of the filter cake closely approximate the experimental values. However, this model is restricted to dead-end filtration which is rarely used in practice and this model is therefore not applicable to crossflow filtration systems. For example, considering Eq. (2.6), one also needs to take into account the lift force, history force, added mass force, etc. (Ghijs, 2014). The assumption of a spatially homogeneous flux is also too straightforward and might influence the rate of local cake layer build-up considerably, as well as the architecture and porosity. Nevertheless, the introduction of a critical friction angle and the correction of the cake porosity with the shape factor of the particles are valuable ideas.

### Pore blocking

A three-dimensional fouling model for the microfiltration of a polydisperse, charged solution was developed by Yoon et al. (1999). An important improvement compared to Lu and Hwang (1993) is the consideration of both pore blocking and cake layer formation. The model allows for the simulation of flux in function of time for any concentration of iron oxide particles, within the validated concentration range.

The effective particle deposition rate is calculated for each particle in the premised particle size distribution (PSD), taking into account both processes that “push” the particle towards the membrane and backtransport processes. This balance takes into consideration: inertia lifting  $v_l$  [ $\text{m s}^{-1}$ ], particle interaction  $v_i$  [ $\text{m s}^{-1}$ ], convection  $v$  [ $\text{m s}^{-1}$ ], diffusion  $v_d$  [ $\text{m s}^{-1}$ ] and shear induced diffusion  $v_s$  [ $\text{m s}^{-1}$ ]. The effective deposition velocity is the difference between the backtransport velocity:

$$v_{\text{tot}}(d_p) = v_d + v_l + v_s + v_i, \quad (2.10)$$

and the velocity toward the membrane  $v$  [ $\text{m s}^{-1}$ ], which is governed by the flux. With  $d_p$  [ $\text{m}$ ] the particle diameter. The gravitational settling velocity  $v_g$  [ $\text{m s}^{-1}$ ] is not included in this balance, so it is assumed that the effect of gravity is negligible. Subsequently, the distribution of particle sizes that are able to deposit on the membrane, given the current flux and backtransport velocity, is given by

$$F_{\text{num}}(t, d_p) = F_{\text{num}}(t_0, d_p) \frac{(J(t) - v_{\text{tot}}(d_p))}{J(t)}, \quad (2.11)$$

with  $F_{\text{num}}(t_0, d_p)$ , the initial particle size distribution.

The cake layer is built up by depositing particles, sampled from  $F_{\text{num}}(t, d_p)$ , one by one on the membrane surface. The particle is dropped from a random location above the membrane. A rolling algorithm is applied whenever a particle comes into contact with a previously settled particle. The rolling continues until a stable position is reached, i.e. the particle touches three already settled particles or the membrane surface. After deposition, the particle is tested for pore blocking (Figure 2.3).

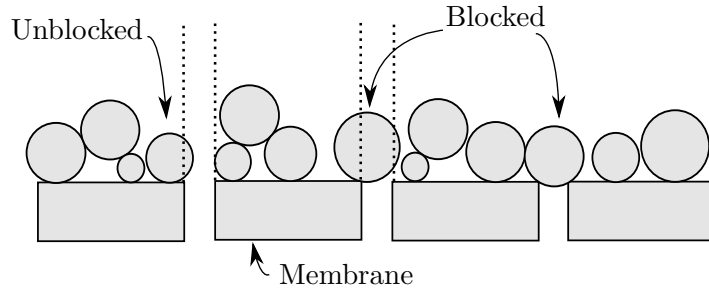


**Figure 2.3:** Pore blocking rule implemented in the model of Yoon et al. (1999). Only particles that touch the membrane surface and are centered within the pore boundaries constitute to pore blocking. Figure adapted from Yoon et al. (1999).

The flux through the membrane is obtained with Darcy's law in conjunction with a RIS model, taking into account the inherent membrane resistance and pore blocking resistance  $R_b$  [ $\text{m}^{-1}$ ]. The latter is computed from

$$R_b = \frac{N_0}{(N - 1)} R_m, \quad (2.12)$$

the flux follows from

$$J = \frac{\Delta p_{t,\text{eff}}}{\nu_f (R_m + R_b)}. \quad (2.13)$$

with  $N_0$  [-] the initial number of membrane pores,  $N$  [-] the free pores. Eq. (2.13) does not contain a resistance term for the cake layer, but its effect is incorporated in  $\Delta p_{t,\text{eff}}$  [Pa] where the pressure drop over the membrane and cake is lowered by the pressure drop over the cake  $\Delta p_c$  [Pa]. The specific surface area and porosity vary with the cake layer depth. Consequently,  $\epsilon$  in the Kozeny-Carman equation (Eq. (2.8)) is not a constant. To deal with this issue, the pressure drop is calculated over different “slices” in a recursive manner (Eq. (2.14), Figure 2.4)

$$\Delta p_T(i+1) = \Delta p_T(i) - \frac{\nu_f \epsilon_i^3 J}{5 S_i^2 (1 - \epsilon_i)^2} \Delta i, \quad (2.14)$$

with  $S_i$  [ $\text{m}^2$ ] the specific surface area of the particles and  $\Delta i$  [m] the thickness of a slice. It is not clear why the Kozeny constant  $k$  is missing from Eq. (2.14).

After applying this scheme to every slice,  $\Delta p_c$  is obtained and the flux across the membrane is computed with Eq. (2.13).

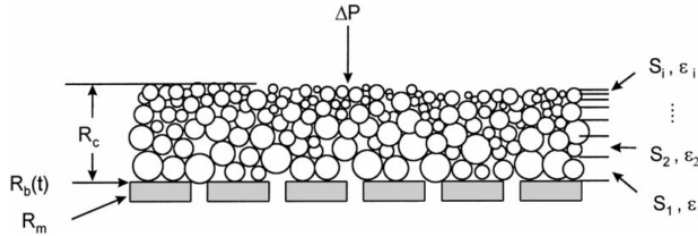


**Figure 2.4:** Representation of the cake layer and the subdivision in different slices  
Yoon et al. (1999).

Each time step, one particle is sedimented on the cake or membrane surface. The elapsed time between two particle depositions is evaluated with Eq. 2.15.

$$\Delta t = ((J(t) - v_{\text{tot}}(d_p)) A_m c_b F_{\text{num}}(t, d_p)) \quad (2.15)$$

with  $A_m$  [ $\text{m}^2$ ] the specific membrane area. In the next time step, Eq. 2.11 is re-evaluated with the new flux and a new particle is sampled from the new PSD.

The model performs quite well in the early stages of the filtration but the prediction accuracy gradually declines with time. The simulated flux evolves to a steady state while experimental values show that the flux keeps decreasing. The authors mention that unfulfilled assumptions for the backtransport equations as the probable cause, but the discrepancy between the simulations and experimental data can also be due to the overestimation of the inertial lift force. The channel inlet velocity is used as the velocity component in this force and this component is overestimated considerably for particles in the slow moving fluid close to the membrane surface. A more involved calculation of the velocity would probably enhance model performance. The added value of this model lies in the introduction of pore blocking in a less empirical manner, the polydispersity and charge interactions.

In the previously discussed models, the filter cake is either assumed spatially homogeneous, with an average value for porosity and thickness, or heterogeneous along the depth. Yet, heterogeneity along the longitudinal axis is never considered. This implies that there is no spatial variation of the filtration resistance and flux. Consequently, these models are not able to account for the spatial heterogeneity of membrane fouling. Li and Wang (2006) propose a sectional approach to deal with this problem.

This sectional method allows the inclusion of turbulence, induced by aeration. The membrane surface is subdivided into different sections with equal length in which the different variables are tracked. The subdivision is along the longitudinal axis of the membrane, in contrast to the method discussed in Yoon et al. (1999), where the “slices” are taken parallel to the membrane.

For simulating the attachment of a sludge particle with a certain diameter ( $d_p$ ) on the membrane surface, two forces are taken into account: the drag force  $F_d$  and the lift force  $F_l$  [N]. The permeate flux drags the particles to the membrane and the lift force, a consequence of the turbulent flow, is the opposing force. The balance between these two forces controls the rate of particle deposition, expressed as a probability of deposition  $E$  [-]:

$$E = \frac{F_d}{F_d + F_l} \quad (2.16)$$

For a probability  $E$ , the rate of biomass attachment becomes,

$$\frac{dM}{dt} = E C J \quad (2.17)$$

with  $c_b$  [ $\text{kg m}^{-3}$ ], the concentration of suspended solids (SS).

The effects of the continuous scouring through aeration is expressed as a rate of detachment described by Eq. 2.18.

$$\frac{dM}{dt} = -K_d M_{sf} \quad (2.18)$$

with  $K_d$  [ $\text{s}^{-1}$ ] the rate coefficient of sludge detachment and  $M_{sf}$  [ $\text{kg m}^{-2}$ ] the mass of sludge in the filter cake.

A Langmuir model is used for  $K_d$ , as it reaches a maximum for a very thick filter cake and decreases with the cake thickness. The rate of detachment is essentially proportional to the shear intensity, biomass stickiness and other properties of the sludge layer. The net rate of sludge accumulation during a certain filtration period is obtained by solving the abovementioned equations for biomass attachment and detachment. Li and Wang (2006) also describe equations for the rate of sludge removal during the idle-cleaning period.

The filtration resistance is calculated using a RIS approach. The total resistance  $R_t$  is the sum of the intrinsic membrane resistance, the resistance of the dynamic and stable cake layer and the pore fouling resistance. All of these resistance terms involve an empirical resistance parameter that needs calibration. Finally, Darcy's law is used to calculate the flux through the different membrane sections. As opposed to other models, sludge detachment is considered and a sectional approach is established to capture the heterogeneity of membrane fouling. However, this model involves a lot of parameters and the article does not provide any information on the calibration.

Due to the many empirically described mechanisms, the performance of the model varies in different operational conditions, which might just indicate that the model does not comprise all relevant processes.

### Cut-off diameter

A one-dimensional model describing the TMP in a submerged hollow fiber membrane is proposed by Broeckmann et al. (2006). The hydrodynamics at the outer side of the membranes are determined through a multiphase flow model for which the details are unfortunately not discussed in the article.

The bulk phase particles are divided into two fractions. The first one is able to enter the pores and constitutes to pore blocking. The other fraction is not able to enter the pores and constitutes to cake layer formation. Mathematically, this is achieved by multiplying the retained weight fraction distribution of the membrane pore size distribution  $R_{\text{pore}}(d_p)$  with the distribution of the bulk particle sizes  $g_b(d_p)$ . For a particle with size  $d_p$  that is approaching a random pore, the probability of the pore being larger than  $d_p$  is given by  $R_{\text{pore}}(d_p)$ . Thus, the PSD of the fraction entering the pores is given by,

$$g_m(d_p) = R_{\text{pore}}(d_p) g_b(d_p). \quad (2.19)$$

Hence, the PSD of the retained solids follows from,

$$g_{\text{cake}}(d_p) = (1 - R_{\text{pore}}(d_p)) g_b(d_p). \quad (2.20)$$

For what concerns pore blocking, it is assumed that every particle able to penetrate the membrane is completely retained within the membrane pores. Hence, the membrane porosity decreases when particles enter the pores. The rate of porosity change is calculated through a mass balance,

$$\rho_{p,m} V_m \frac{d\epsilon_m}{dt} = -J c_m^b A_m, \quad (2.21)$$

with  $V_m$  [ $\text{m}^3$ ] the total membrane volume,  $\rho_{p,m}$  [ $\text{kg m}^{-3}$ ] the density of particles in the membrane pores and  $c_m^b$  [ $\text{kg m}^{-3}$ ] the mass concentration of particles that will penetrate the membrane, based on  $g_m(d_p)$ .

Broeckmann et al. (2006) also employs a RIS approach. The RIS model consists of four resistances; the cake resistance, the intrinsic membrane resistance, the pore blocking resistance and the irreversible resistance. The Kozeny-Carman equation (Eq. 2.8) can be rewritten to relate the membrane resistance to the membrane porosity, obtained from Eq. 2.21,

$$R_b + R_m = \frac{(1 - \epsilon_m)^2 K_p}{(\epsilon_m)^3}, \quad (2.22)$$

where  $K_p$  [ $\text{m}^{-1}$ ] is a membrane specific constant.  $R_c$  is obtained from,

$$\frac{dR_c}{dt} = \frac{dl}{dt} K_c, \quad (2.23)$$

with  $l$  [m] the filter cake thickness and the specific cake resistance  $K_c$ ,

$$K_c = \frac{k_90}{\bar{d}_p^2} \frac{\left(\frac{c_c}{\rho_s}\right)^2}{\left(1 - \frac{c_c}{\rho_s}\right)^3}, \quad (2.24)$$

with  $c_c$  [ $\text{kg m}^{-3}$ ] the mass concentration of the cake layer and  $\bar{d}_p$  [m] the mean diameter of bulk particles.

The cake layer formation is determined through a force balance (Figure 2.5).

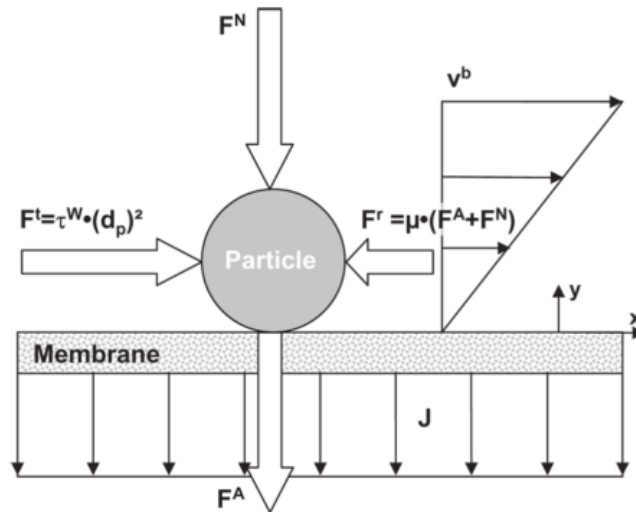


**Figure 2.5:** Considered forces on a particle during filtration (Broeckmann et al., 2006).

$F_t$  [N] is the tangential shear stress resulting from the liquid flow,  $F_\tau$  [N] is the friction force, the normal force  $F_N$  [N] is the drag force resulting from the permeate flux and  $F_A$  [N] is the adhesion force between the particles and the membrane. It is interesting to note that the lift force is not included in this mass balance. All forces point towards the membrane, no backtransport forces are considered to oppose this. With this fact in mind, a particle “sticks” to the surface when the horizontal forces cancel out one another (Eq. 2.25) and

$$\tau_W d_p^2 - \mu_{\max} (F_N + F_A) = 0, \quad (2.25)$$

where  $\tau_W$  [Pa] is the shear stress and  $\mu_{\max}$  [-] is the maximum friction coefficient.

From Eq. 2.25 an equation is derived for the maximum diameter of particles that are able to adhere to the membrane surface, under the current filtration conditions. Particles larger than this cut-off diameter will stay in the bulk phase.

The growth of the cake layer is described by Eq. 2.26.

$$c_c \frac{dl}{dt} = J \omega c_c^b \quad (2.26)$$

with  $\omega$  [-] the bulk concentration of particles that are retained on the membrane surface, i.e. the fraction of  $c_c^b$  [ $\text{kg m}^{-3}$ ] that is smaller than the cutoff diameter and  $c_c$  the mass concentration of the cake layer. Broeckmann et al. (2006) do not specify how  $c_c$  is obtained even though it is a crucial variable/parameter. Hence, it is assumed that  $c_c$  is a parameter that needs calibration.

During backflushing, particles are removed from the cake layer and pores. This process is incorporated through simple, empirical models.

The strength of this model is the implementation of particle and pore size distributions as typically only the former is included. Additionally, the implementation of backflushing processes definitely improves the applicability of this model even though the formulation is simple and empirical. The model however, has a few weaknesses including the lack of a sectional approach, many parameters and the low prediction accuracy when operational conditions differ from calibration conditions. Furthermore, some assumptions that can be valid for hollow fiber membrane systems might be invalid for other types of membrane filtration. The application of the model on these systems is therefore less appealing. Both a strength and a weakness of the model is its focus on constant flux filtration as most models address constant pressure filtration instead.

### Force balance, rolling and backwashing

Cao et al. (2015) elaborates a model to predict the TMP in an MBR that combines the deposition criteria described in Broeckmann et al. (2006) and the particle depositing rules from Yoon et al. (1999) in a RIS.

The cake layer is formed by particles that deposit one by one from a random location within the boundaries of the simulated membrane surface. A particle drops until it reaches the membrane surface or an already deposited particle; of the latter, a rolling algorithm is initiated until a stable position is reached. Each series of particle depositions is defined as a “filtration cycle”. Such a cycle ends when the total volume of deposited particles fulfills,

$$V_{p,m} = \frac{A_m J t_f p_f c_b}{\rho_s}, \quad (2.27)$$

with  $t_f$  [s], the filtration time per filtration cycle and  $p_f$  [-] the total fraction of depositable particles. Eq. 2.27 is a combination of the equations presented in Yoon et al. (1999) and Broeckmann et al. (2006).

The porosity of this newly formed cake layer is evaluated at the end of each filtration cycle and is afterwards modified with a compression factor taking into account compression. With

both the porosity and cake thickness established it is possible to calculate the TMP using a RIS. This model is furthermore extended with a backwashing model simulating cake removal due to air scouring and backwashing *sensu stricto*.

The comprisal of different ideas and concepts results in a good performing model. It also shows the importance of different factors such as PSD, compression and shear stress on the characteristics of the filter cake. This model offers a porosity profile along the cake thickness. Ideally this should be extended with a porosity profile along the cake length. Cake compression is included albeit through a simple compression factor. The authors state the need for a hydrodynamic model in order to provide a more realistic shear stress.

### Biofouling

All of the abovementioned models describe particulate fouling. Nonetheless, it is important to keep in mind that this is not the only fouling type, biofouling has a considerable impact on different systems as this kind of fouling not solely occurs at membranes but also at heat exchangers, pipes, feed spacers, etc. For this reason, a great deal of effort has been put in the modelling of this fouling type. Consequently, these models are generally more advanced than the RIS models mentioned above. Such a model is described in Picioreanu et al. (2009) and Vrouwenvelder et al. (2010). This three-dimensional biofouling model simulates liquid flow, mass transport of a soluble substrate and biofouling in the feed channels of reverse osmosis and nanofiltration systems. The hydrodynamics are modelled via the steady-state Navier-Stokes equations for incompressible laminar flow. The distribution of substrate in the system is obtained through a mass balance. The biofilm is mimicked using an overlaying cellular automaton including terms for growth, decay, convective and diffusive biomass spreading, biomass attachment and detachment.

The simulations results (Figure 2.6) really show the importance of coupling the fouling model with a fluid dynamics model. Figure 2.6 shows that when fouling persists, the fluid flow is redirected and high shear channels form where no fouling occurs.

The authors show that the model is able to accurately predict feed channel pressure drop and biomass accumulation on the feed spacers. The simulated, three-dimensional distribution profiles of biomass and velocity agree qualitatively with the experimental measurements. The implementation of a fouling model in combination with computational fluid dynamics (CFD) is a major improvement towards accurate, mechanistic models. This methodology, implemented for biofouling is also highly relevant for particulate fouling as the fluid flow at the membrane greatly affects cake formation and vice-versa. This approach should be carried out in a sectional framework to incorporate heterogeneous cake formation.

Table 2.1 provides an overview of the processes, fouling types, force balances, etc. that are included in the abovementioned mechanistic models. The processes comprise cake compression, detachment of cake layer/biofilm, backflushing and dynamic fluid simulations. Two

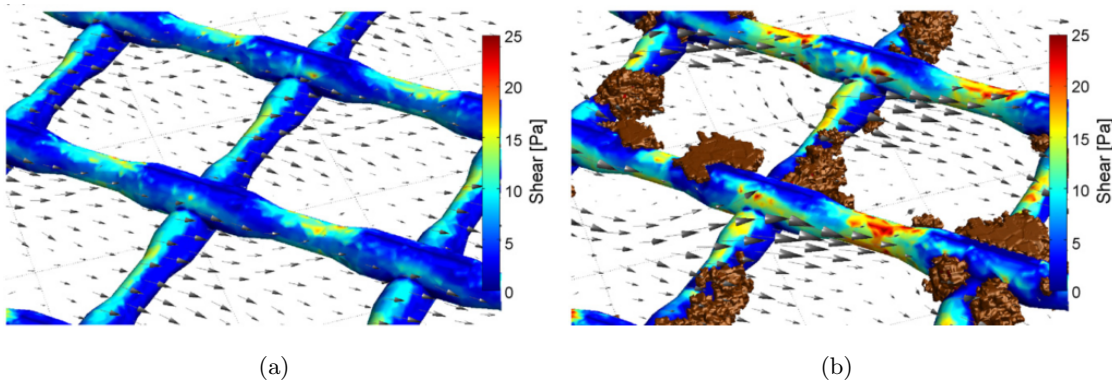


**Figure 2.6:** Distribution of viscous shear and biofilm on the feed spacers for the initial condition (a) and after 2.5 days (b). The arrows show the direction and magnitude of the fluid velocity. The magnitude of the velocity is in the order of  $1 \text{ [m s}^{-1}]$  (Picioranu et al., 2009).

force balances are considered, one for particles in the cake layer and one for particles in the fluid. The fouling types include particulate fouling, pore blocking and biofouling and the spatial heterogeneity of the fouling is taken into account. Also, particle shape corrections and multidispersity of the particles are included in the comparison.

### 2.2.3 Data-driven models

Even though the majority of fouling models are mechanistic, it is important to review some of the data-driven modelling approaches as well. Typically, machine learning is used to fit a model to the experimental data. If sufficient data are available and precautions are taken to avoid overfitting, this type of “black-box” modelling can lead to good results.

In Shetty and Chellam (2003) an artificial neural network was built to predict fouling of flat and spiral-wound nanofiltration membranes. The fouling is quantified in terms of the total resistance to water permeation  $R_t$ , described by Darcy’s law (Eq. 2.1). The input layer consists of different operational and feed water quality parameters that are typically monitored during municipal wastewater treatment, e.g., influent flow rate, permeate flux, operation time, feed water quality parameters, etc. The neural network was trained on an extensive amount of data from different ground and surface water filtration experiments using different membranes to predict the total hydraulic resistance  $R_t$ . In this way, a model was build that predicts membrane fouling in various operational conditions.

Artificial neural networks excel at describing complex nonlinear relationships between input and output variables (Tu, 1996) and are therefore a popular data-driven approach to model membrane fouling with numerous applications described in literature. A summary of these

**Table 2.1:** Overview of the incorporated processes, fouling types, etc. and general details of the advanced mechanistic models.

	<i>Lu and Hwang (1993)</i>	<i>Yoon et al. (1999)</i>	<i>Li and Wang (2006)</i>	<i>Broeckmann et al. (2006)</i>	<i>Cao et al. (2015)</i>	<i>Vrouwenvelder et al. (2010)</i>
<b>Operational mode</b>	DE	CF	CF	CF	CF	FF
<b>Processes</b>						
cake compression	X	X			X	
fouling detachment			X			
backflushing				X	X	
fluid dynamics				X	X	X
<b>Force balance</b>						
fouling layer	X	X	X	X	X	X
fluid						X
<b>Fouling</b>						
particulate	X	X	X	X	X	
pore blocking		X	X	X	X	
biofouling						X
spatial heterogeneity	1D	1D	2D	1D	1D	3D
<b>Other</b>						
particle shape	X					
multidispersity	NM	X	NM	X	X	

NM: not mentioned, DE: dead-end filtration, CF: crossflow filtration, FF: feed channel fouling.

studies can be found in Mirbagheri et al. (2015).

Dalmau et al. (2015) propose the use of model trees in predicting membrane fouling, which combines linear regression with decision trees. Linear regression is a simple technique resulting in a model with high bias but low variance, prone to underfitting nonlinear data. In contrast, decision trees capture nonlinear patterns in the data, giving rise to models with low bias and high variance, making it prone to overfitting (Dalmau et al., 2015). The combination of both approaches leads to decision trees where each “leaf” is a linear model. The model tree developed in the article consists of 35 multivariate linear equations. Each equation predicts the TMP in various operating conditions. Model trees are capable of partially explaining the system, unlike many other data driven methods (Dalmau et al., 2015).

Data-driven models can also be applied from a different point of view, that is membrane state monitoring or fouling mechanism prediction. The former is elaborated by Maere et al. (2012) and uses principal component analysis in combination with clustering to monitor the fouling behaviour of MBR. A distinction is made between three different membrane states; clean, reversibly fouled and irreversibly fouled, allowing for a real-time decision on possible maintenance actions. A similar method is developed in Drews et al. (2009) where the dominant fouling mechanism is identified by fitting different models to the data, each describing different fouling mechanisms. The dominant fouling mechanism follows from the best fitting model. Figure 2.7 presents the results of this approach.

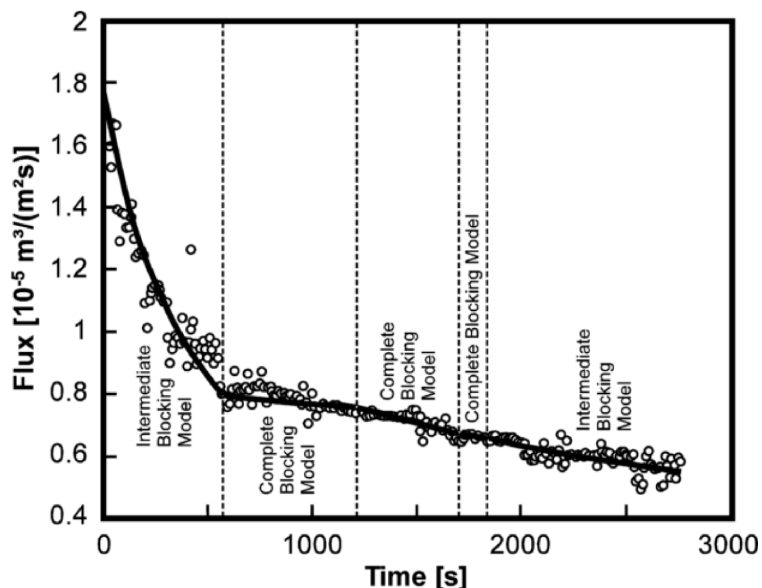


**Figure 2.7:** Comparison between experimental and simulated flux/time curves (Drews et al., 2009).

## 2.3 Profilometry

An important part of this thesis is the development of an experimental setup for the calibration and validation of the spatio-temporal model for filter cake formation. Membrane filtration models are mostly calibrated and validated with data on the TMP and flux during operation. However, considering that the main goal of this model is the characterisation of filter cake formation mechanisms, it is meaningful to gather data about the filter cake properties for a goal-directed calibration/validation. This will be accomplished by a profilometric characterisation of the filter cake.

Profilometry, surface metrology, surface topography, etc. are different terms used in literature to more or less describe the same process i. e. the three-dimensional characterisation of a surface. The distinction between these terms lies in subtleties that are not relevant for this study. These terms are therefore regarded as interchangeable.

Profilometric techniques can be classified in numerous categories, according to the characteristics of the technique. In order to achieve a simple and straightforward classification, a distinction is made between optical methods and non-optical methods. It is nonetheless important to keep in mind that the main goal of this overview is to find a suitable technique for the calibration/validation of the model and not a perfect classification of the profilometric techniques.

### 2.3.1 Non-optical methods

The prominent method in this category is *stylus profilometry (SP)*. In stylus profilometry, the surface is characterised by the interaction of a sensing tip with the sample. The vertical displacement of the tip is recorded while the stylus is moving across the sample's surface (Lonardo et al., 2002). Two main disadvantages of stylus profilometry can be identified (Stout and Blunt, 2000; Lonardo et al., 2002). Firstly, this method is generally quite slow, taking a long time to characterise a small area of the specimen. Secondly, the contact between the instrument and sample can result in the deformation of the sample and an underestimation of the height of soft surfaces. Consequently, stylus profilometry is not suitable for the surface characterisation of a filter cake as it most certainly classifies as "soft".

*Atomic force microscopy (AFM)* is generally not regarded as stylus profilometry because there is no contact with the surface, since it is characterised via repulsive forces exerted on the sensing tip. Nevertheless, the other working principles are quite similar. Atomic force microscopy is mostly used for submicron measurements and its nanometer scale resolution would be excessive for filter cake measurements, which are in the micrometer scale (Whitehouse, 1999).

In *scanning tunneling microscopy (STM)* a metal tip scans the surface of the sample. A voltage is applied over the gap between the tip and the specimen. When the conducting tip is close to the surface, electrons will bridge the gap between the surface and the tip, resulting in a current. Changes in surface height result in changes in magnitude of the current that are subsequently recorded. STM is used for the surface characterisation on an atomic level and is therefore not a suitable technique for this research (Binnig and Rohrer, 1982; Hansma and Tersoff, 1987).

*Scanning electron microscopy (SEM)* utilises a beam of electrons to form a three-dimensional image of the investigated surface. This beam is produced in an electron gunner or electron emitter, accelerated by a set of anodes and focused on the specimen by a series of electromagnets. On collision, one part of the electrons will reflect off the surface, another part excites the atoms of the specimen, thereby producing secondary electrons, and other electrons penetrate the sample producing X-ray radiation. Both types of electrons and the X-rays can be captured by specialised detectors giving rise to a profilometric image when the electron beam is moved over the surface of the sample in a scanning motion (Reimer, 1985; Goldstein et al., 2003).

### 2.3.2 Optical methods

The number of optical methods for the three-dimensional characterisation of a surface is vast. It is impossible to discuss all these techniques, therefore a selection is made of the most distinct types in order to still give a comprehensive overview.

Interferometry is based on the interaction of multiple light beams and uses the superposition of waves to gather information about the surface characteristics (Hariharan, 2012). The number of measurement techniques based on interferometry is enormous. However, the working principle of all these techniques is basically the same. A beam of light, is split by a glass plate with a semi-reflective coating; one beam acts as a reference and is directly reflected via a mirror to the detector while the second beam is reflected on the surface of the sample. These two beams are recombined by the beamsplitter and will interfere. Figure 2.8 presents a schematic overview of such a generic interferometer. Constructive interference is observed when the path length is the same for both beams, giving rise to the interference signal with the largest amplitude and hence the highest intensity. The signal intensity drops with bigger path differences (the difference cannot exceed the wavelength). Consequently, an image is obtained with different intensity values for each pixel. By altering the path length of one of the beams it is possible to scan for other heights in the sample and a profilometric image is formed. For these kind of measurements, white light is mostly used as it produces more accurate results than monochromatic light.

*White light interferometry (WLI)* has a resolution limit of approximately  $0.5 \mu\text{m}$  due to diffraction effects (Conroy and Armstrong, 2005; Hariharan, 2012). Problems can arise from the presence of thin films in the specimen that cause errors in the measurements (Conroy and Armstrong, 2005). Hence, the presence of an aqueous layer in the filter cake poses a potential risk for its profilometric characterisation.

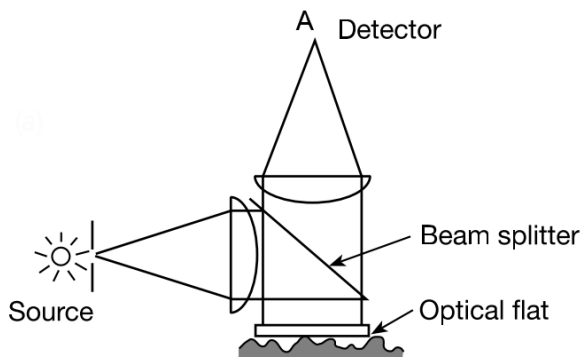


**Figure 2.8:** The basic outline of an interferometer (Whitehouse, 1999).

*Differential interference contrast microscopy (DICM)* or Nomarski microscopy also adopts the principles of interferometry, but both the reference and sample ray go through the sample in two adjacent points. The difference in height of those points translates in a phase shift between both rays. The rays are recombined and the resulting interference is proportional to the difference in path length of the rays. A differential image is obtained of the surface (Khalaf and Bainbridge, 1981).

Other interferometry related methods are *digital holographic microscopy (DHM)* (Kemper et al., 2007) and *optical coherence tomography (OCT)* (Podoleanu, 2012). The working principle of these techniques is very similar to DICM and will therefore not be elaborated.

*Confocal laser scanning microscopy (CLSM)* is basically a conventional light microscope with the ability to illuminate a small section of the sample. The reflected light from the sample is filtered through a pinhole that filters out all the out-of-focus light. Hence, it is possible to illuminate a certain viewing depth, which is not possible with a conventional light microscope. The combination of images from different depths gives rise to a three-dimensional structure (Hocken et al., 2005). This method is technically not a profilometric technique as it actually visualises the internal structures of a specimen. The maximal attainable resolution of confocal laser scanning microscopy is about the same as that of a conventional light microscope (Pawley, 1995). The use of CLSM as a tool for the profilometric characterisation of surfaces is restricted by its low scanning rate and the problems that arise with the occurrence of different optical properties in one specimen (Cha et al., 2000). *Pattern projection profilometry* or structured light profilometry establishes a three-dimensional profile by projecting light patterns on the object and capturing the distortion of the pattern, from a different angle, with a

camera. From an angle, the differences in height of the object results in a phase shift of the projected pattern (Figure 2.9). The captured image is subsequently analysed to calculate the underlying phase distribution. This technique is, along with the interferometric techniques, “indirect” which means that calibration is needed to map the phase distribution to height measurements (Gorthi and Rastogi, 2010). Pattern projection profilometry includes *fringe projection profilometry (FPP)* (Zhang, 2010) and *Fourier profilometry (FP)* (Su and Chen, 2001). Also *Moiré profilometry (MP)* is considered as pattern projection profilometry. This technique projects two light gratings on the object, but the underlying principles are the same (Rössler Tomas et al., 1998).

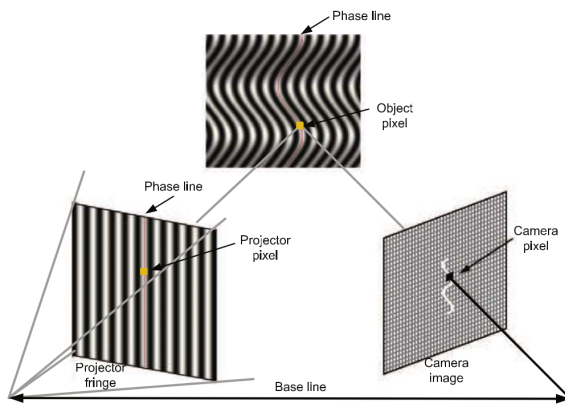


**Figure 2.9:** Illustration of the principle of a digital fringe projection profilometer as an example of the working principle of pattern projection techniques (Zhang, 2010).

In *white light axial chromatism (WLAC)*, a white light source is passed through a concave objective lens. The different refractive indices for each wavelength result in a dispersion of the light beam and each wavelength is refocused at a different distance from the lens. The confocal configuration assures that only the in-focus wavelength reaches the detector for which the wavelength is determined and the corresponding height of the sample is obtained. This technique is insensitive to ambient light and stray reflection, there is no need for vertical scanning to sense the surface height and it is a direct technique. For these reasons, this technique seems to be ideal for the profilometric characterisation of a filter cake (Leach, 2011; Nanovea, 2015). A schematic outline of such a system is presented in Figure 2.10. The lateral resolution limits and relative prices of the different profilometric techniques are denoted in Table 2.2.

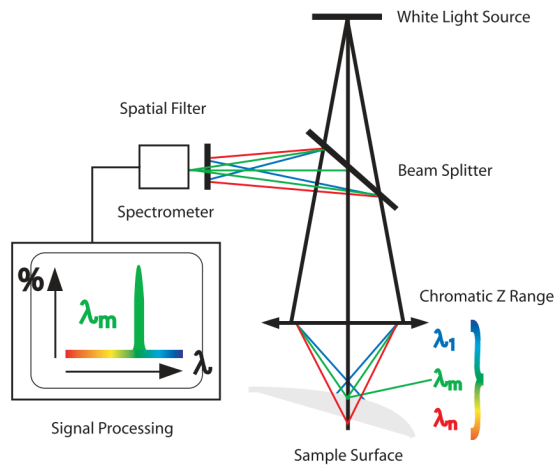


**Figure 2.10:** Schematic representation of a white light axial chromatic confocal profilometer (Nanovea, 2015).

**Table 2.2:** Overview of the lateral resolution and price class of the profilometric techniques. References: Song (1991) [1], Catto and Smith (1973) [2], Conroy and Armstrong (2005) [3], Kemper et al. (2007) [4], Pawley (1995) [5], Nanovea (2015) [6]

	resolution	price	remarks
<b>Non-optical</b>			
SP	0.5 μm [1]	\$	dependent on the stylus size
AFM	0.1 nm [1]	\$\$	
STM	0.1 nm [1]	\$\$	
SEM	1 nm [2]	\$\$\$	
<b>Optical</b>			
<b>Interferometry</b>			
WLI	0.5 μm [3]	\$	diffraction limited
DICM	0.5 μm	\$	
DHM	0.5 μm	\$	good axial resolution (5 nm) [4]
<b>Focus detection</b>			
CLSM	< 0.5 μm [5]	\$\$	close to diffraction limit
<b>Pattern projection</b>			
<b>Other</b>			
WLAC	1 μm [6]	\$	supermicron measurements

# CHAPTER 3

## Spatio-temporal model of filter cake formation

The general framework for the spatio-temporal model of filter cake formation, established by Ghijs (2014), has an Euler-Langrangian structure with two model layers (Figure 3.1). The dispersed phase is modelled through a Lagrangian approach where each particle and its modelled quantities (velocity, forces, etc.) are individually tracked by a moving frame of reference (agent-based model (ABM)). The continuous phase is modelled through computational fluid dynamics for which a stationary, Eulerian reference frame is adopted. This chapter will first summarise the assumptions of the model developed by Ghijs (2014) and justify the revision of these assumptions to account for the model extensions. In the remainder, each of the model layers will be elucidated in order to have a thorough understanding of the model before it is extended in Chapter 4.

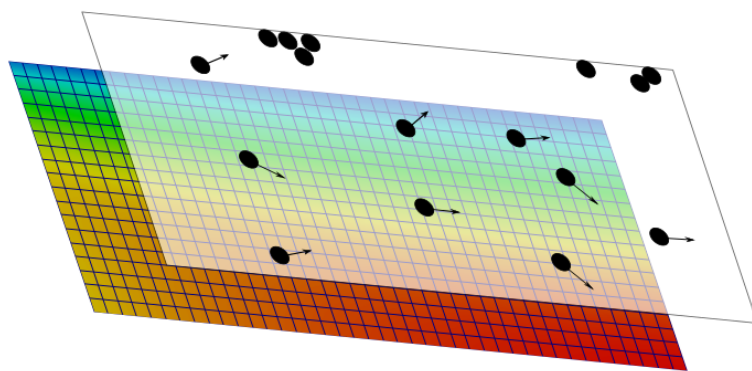


**Figure 3.1:** Schematic representation of the model layers (Ghijs, 2014).

### 3.1 Assumptions

This study aims to develop a model that describes filter cake formation in MBRs as realistically as possible. It is nevertheless necessary to simplify certain processes in order to reduce the computational demands and avoid the overcomplication of the model (Bender, 2000). Therefore, assumptions were made in Ghijs (2014) about the nature of the particles and the system in which they are modelled. Some of these assumptions are well-founded and will be retained here, while others are revised and the model is extended with the necessary processes to account for the extra complexity.

A first assumption is that all particles in the system are **rigid** and **perfect spheres**. This originates from the force balance on the particles as some of these equations are derived for rigid, perfect spheres in a flow field. This assumption might seem too simplistic, but in a bottom-up modelling approach this is a good starting point. It is also assumed that all particles are of the **same size with diameter  $d_p$** . For most of the filtration processes the dispersed phase is made up of particles of different sizes and shapes and monodisperse solutions are rare. Moreover, polydispersity has a significant impact on filter cake formation and this assumption is therefore relaxed in this study. The corresponding model extension involves a considerable programming effort as the implementation was strongly relying on the assumption of monodispersity. This extension is discussed in Chapter 4.

There is **no interaction** of free moving particles **in the bulk phase**. Hence, there are no collisions and free moving particles do not exert forces on each other. Coagulation of free moving particles is consequently not considered. This assumption is justified, given the fact that this model is constructed for laminar flows and the number of particle collisions in the bulk fluid is limited.

The system is modelled in **two dimensions**, the forces and velocities describing the movement of the particles in the bulk phase and the partial differential equations (PDEs) governing the fluid behaviour are described in the  $x$ - and  $y$ -direction. In Ghijs (2014) it was assumed that adding a third dimension would not impact the simulation results significantly so for computational efficiency this dimension was left out. This assumption is also revised in this study as simulation results in two dimensions showed an unrealistic “piling” of the particles in the filter cake. The addition of a third dimension might resolve this issue and a system modelled in three dimensions is more generic.

The **flow profile** of the fluid **is only computed once** at the beginning of the simulation. This assumption implies a steady-state flow of the continuous phase throughout the entire simulation, so that the formation of filter cake on the membrane surface has no effect on the liquid flow profile. This “one-way” assumption is further discussed in Chapter 6 as it is expected that the formation of filter cake greatly influences the liquid flow in close proximity to the filter cake (Picioreanu et al., 2009). This, in turn, will have an impact on the filter cake

formation and for the accurate representation of this process, the model needs to be extended with a bidirectional coupling between the two model layers.

Concerning filter cake formation as such, particles attach with a probability that is inversely proportional to their absolute velocity (section 4.1.2) and attached particles **cannot detach**, regardless of the shear stresses induced by the continuous movement of liquid over the filter cake surface. This shortcoming is partially compensated by the abovementioned adhesion probability. However, a complete force balance that supports detachment of particles from the cake layer will lead to more realistic simulation results (Chapter 6).

The **flux through the membrane is assumed to be constant** in space and time. As the formation of a filter cake layer on top of the membrane results in an increased filtration resistance, the flux is expected to change locally according to the fouling intensity in constant flux membrane filtration systems. The flux will be higher in “cleaner” regions and lower in heavily fouled regions. Hence, it is necessary to extend the model to account for this, which is discussed in Chapter 6.

## 3.2 Dispersed phase

The Lagrangian model of the dispersed phase consists of a system of differential equations that describes a force balance of the free moving particles. The particle’s velocity is determined at every time step and is expressed relatively with respect to the fluid velocity, i.e.  $\mathbf{U}_r = \mathbf{U}_p - \mathbf{U}_c$ , with  $\mathbf{U}_p$  [ $\text{m s}^{-1}$ ] the relative velocity of the particle and  $\mathbf{U}_c$  [ $\text{m s}^{-1}$ ] the local fluid velocity. Newton’s second law is used to determine the particle velocity and follows from (Wörner, 2003; Ghijs, 2014):

$$m_p \frac{d}{dt} \mathbf{U}_p(t) = \vec{\mathbf{F}}_{\text{surf}} + \vec{\mathbf{F}}_{\text{body}}, \quad (3.1)$$

with  $m_p$  [kg] the particle mass. The force balance is divided in body forces  $\vec{\mathbf{F}}_{\text{body}}$  [N] that are distributed over the entire volume of the particle and surface forces  $\vec{\mathbf{F}}_{\text{surf}}$  [N] that act on the surface of the particles (Figure 3.2). For a particle immersed in a fluid, gravity  $\vec{\mathbf{F}}_g$  [N] is the only body force. The surface forces originate from (Wörner, 2003; Ghijs, 2014):

- $\vec{\mathbf{F}}_{\text{Arch}}$  [N] the Archimedes force;
- $\vec{\mathbf{F}}_p$  [N] the force induced from the pressure gradient  $\nabla p$ ;
- $\vec{\mathbf{F}}_{\text{hydr}}$  [N] the resulting hydrodynamic force, which consists of:
  - $\vec{\mathbf{F}}_{\text{drag}}$  [N] the drag force that minimises the difference between fluid velocity and the particle velocity;
  - $\vec{\mathbf{F}}_{\text{am}}$  [N] the added mass force that accelerates the fluid surrounding the particle;

- $\vec{F}_{\text{hist}}$  [N] the history force, which originates from the lagging fluid boundary layers surrounding the accelerating particle;
- $\vec{F}_{\text{lift}}$  [N] the lift force, describing shear lift that is caused by the inertia effects in the viscous flow around the particle.

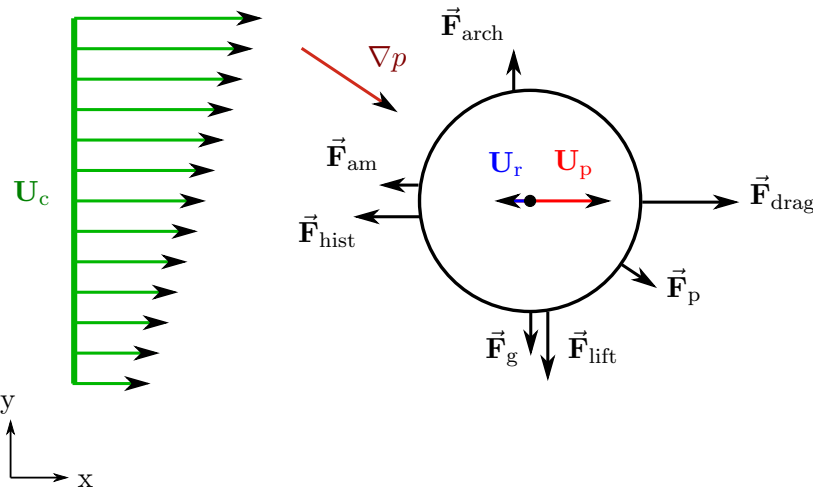


**Figure 3.2:** Schematic representation of the forces that act on free moving particles in a fluid, a negative  $\mathbf{U}_r$  is assumed for the direction of the forces (Ghijs, 2014).

The total force balance on the particle can be written as:

$$\vec{F}_{\text{tot}} = \vec{F}_g + \vec{F}_{\text{arch}} + \vec{F}_p + \vec{F}_{\text{drag}} + \vec{F}_{\text{am}} + \vec{F}_{\text{hist}} + \vec{F}_{\text{lift}}. \quad (3.2)$$

Now, the acceleration of the particles can be derived from Newton's second law (Eq. (3.1)). However, this approach does not take into account the effects of stationary fluid boundaries at the membrane surface. Faxén (1922) proposes the addition of a correction factor to include these effects. Introducing the Faxén correction factor in Eq. (3.2) results in the Maxey-Riley equation for the overall force balance on a particle submersed in a fluid (Maxey and Riley, 1983):

$$\begin{aligned} m_p \frac{d}{dt} \mathbf{U}_p(t) = & -3\pi\eta d_p \left( \mathbf{U}_r - \frac{1}{24} d_p^2 \nabla^2 \mathbf{U}_c \right) + (m_p - V_p \rho_f) \mathbf{g} \\ & - \frac{1}{2} V_p \rho_f \left( \frac{d\mathbf{U}_r}{dt} - \frac{1}{40} d_p^2 \frac{d}{dt} (\nabla^2 \mathbf{U}_c) \right) \\ & - V_p \nabla p - \frac{3}{2} \sqrt{\pi\eta\rho_f} d_p^2 \int_0^t \frac{d\mathbf{u}(\tau)/d\tau}{\sqrt{t-\tau}} d\tau \\ & - 1.615 \rho_f d_p^2 \left( \mathbf{U}_r - \frac{1}{24} d_p^2 \nabla^2 \mathbf{U}_c \right) \sqrt{\mu_f |\kappa|} \operatorname{sgn}(\kappa), \end{aligned} \quad (3.3)$$

with  $\mathbf{u} = \mathbf{U}_r - \frac{1}{24}d_p^2\nabla^2\mathbf{U}_c$  in the history term,  $V_p$  [ $m^3$ ] the particle volume and  $\kappa$  [ $s^{-1}$ ] the fluid velocity gradient defined as,

$$\kappa_i = \frac{d\mathbf{U}_{c,j}}{di} \quad (3.4)$$

where  $i$  and  $j$  represent directions in a two-dimensional Cartesian coordinate system.

### 3.3 Filter cake formation

By solving Eq. (3.3) one can accurately simulate the behaviour of the dispersed particles for a given fluid flow profile. The first step in modelling the filter cake formation is the detection of collisions of particles with the already formed cake layer or the membrane surface. This is accomplished with a collision detection algorithm which is detailed in Chapter 4. To ensure that not all collisions of the particles with the filter cake result in adhesion, this process is governed by a probability. This function defines the probability  $P(\mathbf{U}_p)$  [-] for a particle to attach to the filter cake in the event of a collision and is inversely proportional to the particle's momentum:

$$P(\mathbf{U}_p) = e^{-k\mathbf{U}_p}, \quad (3.5)$$

with  $k$  [-] a parameter representing the “stickiness” of the particles which needs to be determined experimentally. Equation (3.5) is the only empirical equation and does not fit in the model's mechanistical mindset. Its role, however, is temporary and will become redundant when a full force balance is in place for particles in the filter cake (chapter 6).

### 3.4 Continuous phase

This model layer describes the behaviour of the continuous phase as it flows continuously into the filtration unit via the inlet and is discharged at the outlet and through the membrane pores.

#### 3.4.1 Fluid dynamics

The continuous phase is modelled through an Eulerian approach, the control volume is included in a stationary reference frame and the flow quantities such as velocity and pressure are described for each fixed point inside this control volume. The flow pattern and fluid velocities of the continuous phase are obtained by solving the mass, momentum and energy conservation equations, written as a set of PDEs. Depending on the fluid characteristics of the modelled system, such as the rheology and flow regime (turbulent/laminar flow, single phase/multiphase system), different sets of PDEs are used (Versteeg and Malalasekera, 1995; Ranade, 2002).

The first equation describes the conservation of mass within a given volume  $\Omega$  [ $\text{m}^3$ ] and is based on the following axiom: the rate of increase of mass in a fluid element is equal to the net rate of flow into the fluid element since no mass can be created or destroyed, assuming incompressibility. So,

$$\frac{\partial \rho_f}{\partial t} + \nabla(\rho_f \mathbf{U}_c) = 0, \quad (3.6)$$

with  $\mathbf{U}_c$  [ $\text{m s}^{-1}$ ] the fluid velocity in the volume  $\Omega$  and  $\rho_f$  [ $\text{kg m}^{-3}$ ] the density. The compressibility is negligible for most liquids and  $\rho$  can be assumed as constant. Consequently, for incompressible fluids (Versteeg and Malalasekera, 1995):

$$\frac{\partial \rho_f}{\partial t} = 0, \quad (3.7)$$

and

$$\nabla(\rho_f \mathbf{U}_c) = \rho_f \nabla \mathbf{U}_c, \quad (3.8)$$

so that

$$\nabla \mathbf{U}_c = 0. \quad (3.9)$$

The conservation of momentum, as a second equation, is governed by a force balance acting on  $\Omega$ . By taking into consideration the body forces such as gravity and the surfaces forces such as the compressive force and friction force and inserting them into Newton's second law of motion, one obtains:

$$\rho_f \left( \frac{\delta \mathbf{U}_c}{\delta t} + \mathbf{U}_c \cdot \nabla \mathbf{U}_c \right) = -\nabla p + \nabla \cdot \tau + f, \quad (3.10)$$

with  $\tau$  [N] the viscous stress tensor and  $f$  [ $\text{N m}^{-1}$ ] the external body forces. In most of the cases,  $f$  only consists of the gravitational force (Versteeg and Malalasekera, 1995; Ranade, 2002).

For an incompressible, Newtonian fluid the viscous stresses are proportional to the rates of deformation and constant viscosity can be assumed. Consequently, the stress tensor  $\tau$  in Eq. (3.10) can be written in terms of the viscosity  $\mu_f$  and fluid velocity, leading to the Navier-Stokes equation for incompressible flow (Versteeg and Malalasekera, 1995),

$$\rho_f \left( \frac{\delta \mathbf{U}_c}{\delta t} + \mathbf{U}_c \cdot \nabla \mathbf{U}_c \right) = -\nabla p + \mu_f \nabla^2 \mathbf{U}_c + f. \quad (3.11)$$

For this study, an isothermal flow is considered and the equations for the conservation of energy are not relevant and are therefore not discussed. The set of PDEs (3.9) and (3.11) is called the Navier-Stokes system for incompressible flow (Versteeg and Malalasekera, 1995).

### 3.4.2 Computational fluid dynamics

The Navier-Stokes equations provide an accurate theoretical basis for modelling dynamic fluid behaviour. However, these equations are complex, non-linear and coupled, making the solution quite complex and in practice more often than not, analytical solutions are non-existent. It is therefore necessary to use numerical methods in order to obtain a solution for the modelling problem at hand, which is the scientific domain of CFD (Ranade, 2002).

*“Computational fluid dynamics is a set of numerical methods applied to obtain approximate solutions of problems of fluid dynamics and heat transfer.”*

— (Zikanov, 2010)

Depending on the characteristics of the fluid in the system, different fluid dynamics equations need to be used. The Navier-Stokes equations (3.9) and (3.11) are derived for a Newtonian, incompressible fluid in an isothermal system which is a good representation for modelling wastewater and other liquids used in membrane filtration systems.

After selecting the appropriate flow equations and boundary conditions, the equations are discretised either using finite volume methods (FVMs) or finite element methods (FEMs). The FEM is not used in this work and is therefore not elucidated.

In the FVM, the domain is subdivided into a finite number of cells with a certain volume, where the values of the different variables are integrated values of their respective cells, stored in the center points of the cells. The discretised PDEs are obtained by constructing the conservative form for which volume integrals are used for the conservative components and surface integrals of the divergence terms (Ranade, 2002; Patankar, 1980). For a scalar property  $\phi$ , the discretised transport equations can be written as follows:

$$\int_t^{t+\Delta t} \left( \int_V \frac{\delta(\rho \phi)}{\delta t} dV + \int_S \rho U \phi \cdot n dS = \int_S \Gamma \nabla \phi \cdot n dS + \int_V S_\phi dV \right) dt, \quad (3.12)$$

with  $\Gamma$  the diffusion coefficient and  $S_\phi$  the source of  $\phi$ . The first term in Eq. (3.12) denotes a temporal derivative and is zero for the steady-state solution. The second term describes the convective flux of  $\phi$  through the control volume. The third and fourth term, respectively, represent diffusion and the volumetric sources and sinks of  $\phi$  that cannot go under the first three terms. A solution for the flow problem can be obtained by applying Eq. (3.12) to every cell in the discretised spatial domain, and utilising a numerical solving method (Ranade, 2002).



# CHAPTER 4

## Model development

The profound study of other membrane fouling modelling approaches described in literature (Chapter 2) and the critical analyses of the assumptions and model framework proposed by Ghijs (2014) (Chapter 3) identified the processes that require further development and those that are not yet incorporated. The proposed model extensions include changes in the model framework, *sensu strictu*, and the development of accessory tools such as a graphical user interface (GUI) for the analysis of the simulation results and post-processing. This chapter discusses the implemented model extensions and tools in-depth and is concluded by an overview of the model's architecture.

### 4.1 Polydispersity

Broeckmann et al. (2006) demonstrate the influence of particle and membrane pore size distributions on cake layer formation and pore blocking. Meng et al. (2006) also identify the PSD as an important factor that affects membrane fouling. Moreover, it is generally known that a heterogeneous mixture of particle sizes gives rise to a closer packing of particles in the filter cake, which has an important impact on the filtration resistance. It is expected that a dense filter cake is more resilient towards liquid shear stresses and thus less prone to detachment.

It is clear that characterising the feed flow of filtration processes as a homogeneous and monodisperse suspension of perfect spheres is not realistic. The strong dependency of the filter cake architecture and characteristics on the particles size demonstrates the importance of a more accurate representation of the dispersed phase. Extending the model towards polydispersity of the bulk phase is therefore a crucial step in establishing a realistic membrane fouling model. The extension of the model towards polydispersity is somewhat complicated as many processes described by the model, e.g. the attachment of particles, are dependent on the particle diameter and the model implementation often relies on the assumption of

monodispersity. Hence, this modification required the revision and adaptation of some process implementations.

The flocculation of free moving particles in the bulk phase is not considered by this model. Although, the inclusion of polydispersity makes it possible to account for particle aggregates by representing sludge flocs as one particle with a bigger diameter. It is also possible to model non-spherical particles as a multidisperse aggregate of spheres (Hubbard, 1996).

#### 4.1.1 Particle sampling

For a monodisperse stream of particles entering the membrane filter, the number of particles entering each time step  $N$  [-] is given by,

$$N = 6 \frac{\mathbf{U}_{\text{cf}} c_b A}{\rho_s \pi d_p^3} \Delta t, \quad (4.1)$$

with  $\mathbf{U}_{\text{cf}}$  [ $\text{m s}^{-1}$ ] the crossflow velocity at the inlet,  $A$  [ $\text{m}^2$ ] the inlet surface area and  $\Delta t$  [s] the elapsed time per time step.

When modelling a multidisperse bulk phase, Eq. (4.1) does not hold as  $d_p$  is not constant. In order to have a quantitative measure of incoming particles, this flow is expressed as a mass flow rate,

$$\frac{dm}{dt} = \mathbf{U}_{\text{cf}} c_b A, \quad (4.2)$$

with  $m$  [kg] the mass of incoming particles. Multiplying Eq. (4.2) with the total simulation time  $t_{\text{tot}}$  [s] results in an estimated value of the total mass inflow during the entire simulation,

$$m_{\text{tot}} = \mathbf{U}_{\text{cf}} c_b A t_{\text{tot}}. \quad (4.3)$$

The next step is the development of a sampling procedure to represent the multidisperse feed flow, characterised by a PSD. Particles are sampled from this PSD until the total mass, as determined by Eq. (4.3), is attained.

A PSD depicts the relative amount of particles present in the bulk phase as a function of the particle size, based on volume or number. Experimentally determined PSDs are based on a finite number of measurements, making  $d_p$  a discrete variable for which the inverse cumulative distribution function (CDF) sampling algorithm is the most efficient pseudo-random number generator, given a cumulative PSD. This sampling procedure randomly generates a number in the interval [0,1] and searches in the given PSD for the diameter value that corresponds to the probability value that is the closest to the generated number. It can be proven that for a large number of samples, this procedure results in the original PSD.

Lastly, the number of particles that enters each time step is simulated stochastically. For

a sufficiently small time step  $\Delta t$ , the average number of particles entering each step (Eq. (4.1)) is smaller than one. As it is not possible to introduce a non-integer number of particles, the latter represents the probability of a particle entering on a certain time step, this procedure is depicted in Algorithm 1.

---

**Algorithm 1:** Stochastic implementation of the number of particles entering the system.

---

Calculate average number of incoming particles per time step;

```

for  $i = 1$  to number of time steps do
    if random number  $[0,1] < \text{number of particles per time step}$  then
        | 1 particle enters system;
    else
        | No particles enter system;
    end
end
```

---

When considering the introduction of a dispersion into a tubular system with a fully developed parabolic flow, the particles should not be equally distributed across the inlet, since they would then accumulate in the regions with low velocities close to the boundaries and diminish in the middle regions with high velocities, creating a parabolic concentration profile. This phenomenon is shown in Figure 4.1 (b). In order to prevent such an unrealistic behavior, the inlet positions of the particles are determined by a sampling procedure so that the introduction of particles at a certain position is corrected for the local variation in the fluid velocity. This is accomplished by first normalising the parabolic velocity profile at the inlet so that it sums up to one, yielding a proper probability mass function (PMF). The PMF is integrated and the resulting CDF can be used in the above-mentioned inverse CDF sampling procedure. However, this inverse CDF sampling procedure can be computationally demanding for discrete distributions with a lot of bins. The latter is relatively low for the PSD but for the velocity profile this number is too high, resulting in an inefficient sampling procedure which slows down the model considerably. Hence, a power law ( $f(x) = a x^b$ ) is fitted to the CDF and the inverse CDF is determined analytically (Figure 4.2). This approach gives rise to a faster sampling procedure than its discrete counterpart. Figure 4.1 shows the simulation of particles entering a fully developed parabolic flow with and without the parabolic sampling procedure.

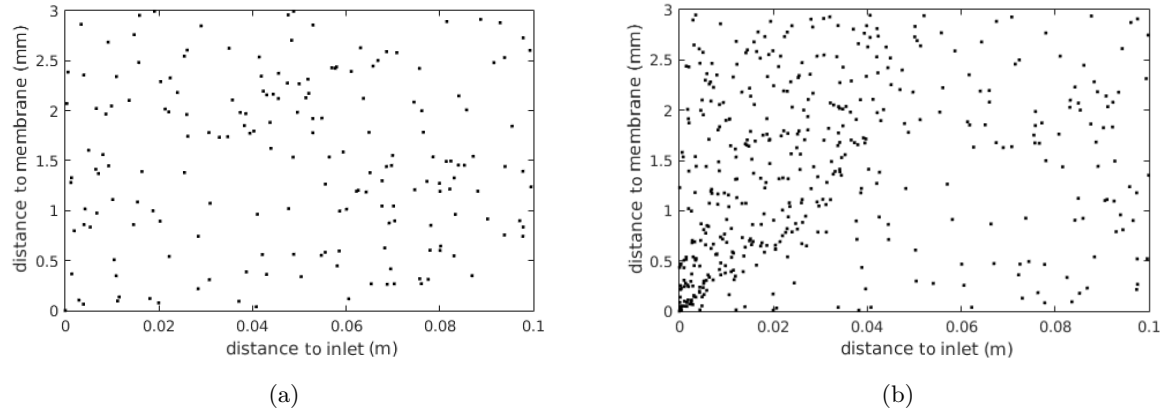


**Figure 4.1:** Simulated flow of particles close to the wall of a tube with a diameter of 8 mm. The incoming particles are sampled with (a) and without the velocity correction (b).

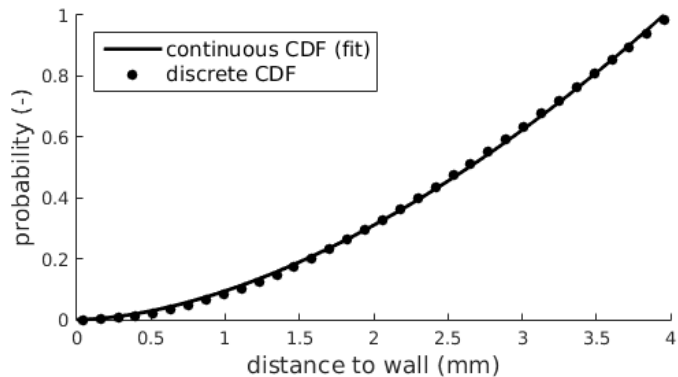


**Figure 4.2:** Comparison of the fitted power law ( $f(x) = ax^b$ ) and the discrete CDF.

### 4.1.2 Filter cake formation

Another consequence of a variable particle diameter is the necessity to modify the collision detection algorithm, registering collisions of particles with the membrane or the filter cake. In Ghijs (2014), the filter cake is implemented in a discrete manner such that the filter cake thickness is tracked at a predefined longitudinal resolution. However, as the filter cake is built up out of spherical particles, the surface is highly irregular and curvy. In order to accurately represent this surface in a discrete way, the discretisation step should be at least one order of magnitude lower than the smallest particle diameter. Hence, storing filter cake thicknesses explicitly is only computationally efficient when considering a thick cake layer. Furthermore, for the evaluation of certain filter cake characteristics such as porosity, segregation and the

PSD, it is better to store the position and the diameter of the filter cake particles, instead of the thickness. The filter cake formation algorithm was thus completely revised to step away from this explicit and discrete representation. This required the development of a collision detection algorithm to detect collisions between spheres instead of collisions between spheres and a surface; this procedure is denoted below.

Tracking all collisions within the system is computationally demanding and would be responsible for a large part of the computing time. In order to keep the simulation time reasonable, it is important to implement this procedure as efficiently as possible. First, a boundary layer  $b$ , whose thickness is the sum of the maximal filter cake thickness  $\Delta l_{\max}$  and maximal particle diameter  $d_{p,\max}$ , is considered (Figure 4.3). Only particles within this boundary layer are close enough to the filter cake and are checked for collision. Next, the deposition trajectory  $\vec{V}$  is constructed between the particle's old and new position along with two other parallel vectors ( $\vec{c}_1$  and  $\vec{c}_2$ ), defining the search range for collision. These vectors represent the position of the biggest particles ( $d_p = d_{p,\max}$ ) that are just able to touch the depositing particle along its trajectory towards the membrane. Consequently, all particles centered outside this band are not able to collide with the depositing particle and are not considered. Finally, collision is detected by evaluating Eq. (4.4) for a predetermined number of points along the deposition trajectory  $\vec{V}$ .

$$\sqrt{(x_1 - x_2)^2 + (y_1 - y_2)^2} \leq (d_1/2 + d_2/2), \quad (4.4)$$

with  $x_1, x_2$  and  $y_1, y_2$  respectively the coordinates of the downward moving particle and the particle in the filter cake and  $d_1, d_2$  the diameter of these particles. If Eq. (4.4) is valid for a node in the collision trajectory, a collision occurs and the particle will attach to the filter cake at that position, if the stochastic adhesion criterion Eq. (3.5) is fulfilled.

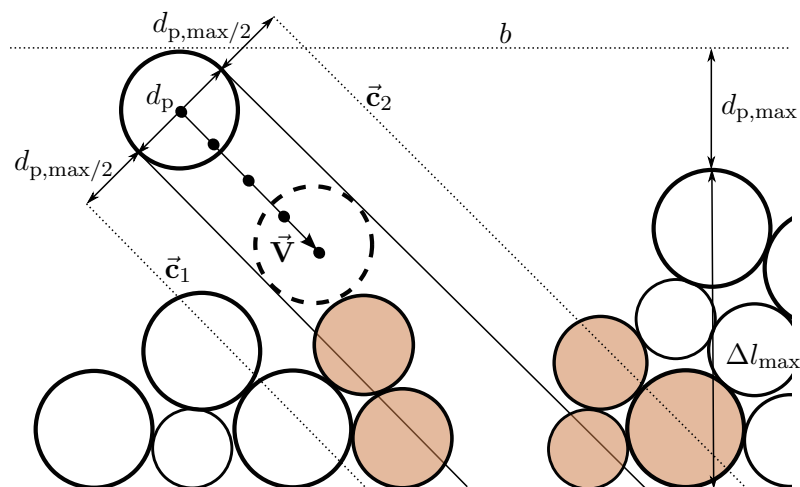


**Figure 4.3:** Schematic representation of the collision detection algorithm. The white particles are outside the collision boundaries and are not evaluated for collision.

To summarise, the new collision detection algorithm is more accurate due to the continuous and implicit representation of the filter cake and its performance is improved by constraining the detection of collisions to a boundary layer and limiting the search for possible collisions in a narrow zone spanning the collision search band.

## 4.2 Extension to a three-dimensional model

The model extension from two dimensions to three dimensions is a logical step towards a realistic filter cake representation. Yet it leads to a considerable increase in the number of modelled particles and one may wonder whether the added value of process knowledge outweighs the extra computational burden. There are, however, two key reasons to chose for a three-dimensional model.

In Ghijs (2014), the simulations suffered from an unrealistic “piling” of particles in the filter cake. Even with the possibility of an elastic collision, it was observed that most particles are caught by previously formed filter cake patches. Due to the lack of a third dimension, a piece of filter cake will catch all incoming particles and keep growing as there is no mechanism that counteracts this. It is hypothesised that by extending the model to three dimensions, a single piece of filter cake will have less impact on the further development of the fouling. Nonetheless, the increased dimensionality will most likely not entirely solve this issue; to do so, the model should be extended with a rolling algorithm. Such an algorithm is described in Cao et al. (2015) and simulates the three-dimensional rolling of spheres. To include this in the model, a transition to three dimensions is imperative.

As can be expected, the flow of particles in a three-dimensional flow field is similar to that in a two-dimensional flow field. Still, it is necessary to modify some of the implemented processes. First, the force balance (Eq. (3.3)) is extended with a third direction ( $z$ ). The resulting force in this direction is not influenced by  $\vec{F}_g$  and  $\vec{F}_{\text{arch}}$  and can be written in terms of  $\vec{F}_p$ ,  $\vec{F}_{\text{drag}}$ ,  $\vec{F}_{\text{am}}$ ,  $\vec{F}_{\text{hist}}$  and  $\vec{F}_{\text{lift}}$ .

Secondly, the lift force in the  $x$ - and  $y$ -direction has to be extended with an additional gradient in the  $z$ -direction. In two dimensions, the inertial lift force has one component in both the  $x$ -direction and  $y$ -direction (Saffman, 1965):

$$\vec{F}_{\text{lift},x} = -1.615 \rho_f d_p^2 U_{r,x} \sqrt{\mu_f \left| \frac{dU_{r,x}}{dy} \right|} \text{sign} \left( \frac{dU_{r,x}}{dy} \right), \quad (4.5)$$

$$\vec{F}_{\text{lift},y} = -1.615 \rho_f d_p^2 U_{r,y} \sqrt{\mu_f \left| \frac{dU_{r,y}}{dx} \right|} \text{sign} \left( \frac{dU_{r,y}}{dx} \right), \quad (4.6)$$

with  $U_{r,x}$  and  $U_{r,y}$  the relative particle velocity in the  $x$ - and  $y$ -direction respectively .

In three dimensions, Eqs. (4.5) and (4.6) need to be extended with a gradient in the  $z$ -direction. The  $x$ -component of the lift force, for example, should now be written as:

$$\vec{F}_{\text{lift},x} = -1.615 \rho_f d_p^2 U_{r,x} \left[ \sqrt{\mu_f \left| \frac{dU_{r,x}}{dy} \right|} \text{sign} \left( \frac{dU_{r,x}}{dy} \right) + \sqrt{\mu_f \left| \frac{dU_{r,x}}{dz} \right|} \text{sign} \left( \frac{dU_{r,x}}{dz} \right) \right]. \quad (4.7)$$

With the correct force balance established, the model is now capable of describing the particle's motion in a three-dimensional flow field.

The adaptation of the filter cake formation process for three dimensions is straightforward. More precisely, the collision trajectory vector is described in three dimensions and the collision search boundaries are now represented by a cylinder. In spite of these changes, the main working principle remains the same.

### 4.3 Parallelisation

As mentioned in Section 4.2, the extension to three dimensions comes at a higher computational expense. For a  $10 \text{ kg m}^{-3}$  dispersion of  $50 \mu\text{m}$  particles ( $\rho_p = 1000 \text{ kg m}^{-3}$ ) flowing in a two-dimensional tube ( $10 \text{ cm} \times 10 \text{ mm}$ ), approximately  $8 \times 10^8$  particles have to be processed each second of simulated time, excluding the particles in the filter cake. When considering a box with the same dimensions and a width of  $5 \text{ mm}$ , this number increases to  $8 \times 10^{10}$ , which indicates the difficulty of maintaining a reasonable simulation time to computational time ratio (SCR). For one processor, the SCR is in the order of  $1 \times 10^{-4}$ . The implementation of the filter cake formation, sampling procedures and force balance are already very efficient, leaving little room for optimisation. Hence, the best solution is to parallelise the implementation to enable simultaneous computation on multiple processors (cores). This is done by assigning every processor a part of the spatial domain, so that it performs the calculations for the particles present in that part. Every predefined number of time steps, information is exchanged between the cores and the particles that moved to a neighbouring part of the spatial domain are reallocated to the appropriate cores. In this way, a good SCR ( $\sim 1 \times 10^{-3}$ ) is obtained without the need of convoluted code optimisation.

### 4.4 Model architecture

The overall model architecture is depicted in Figure 4.4. The model takes three inputs,

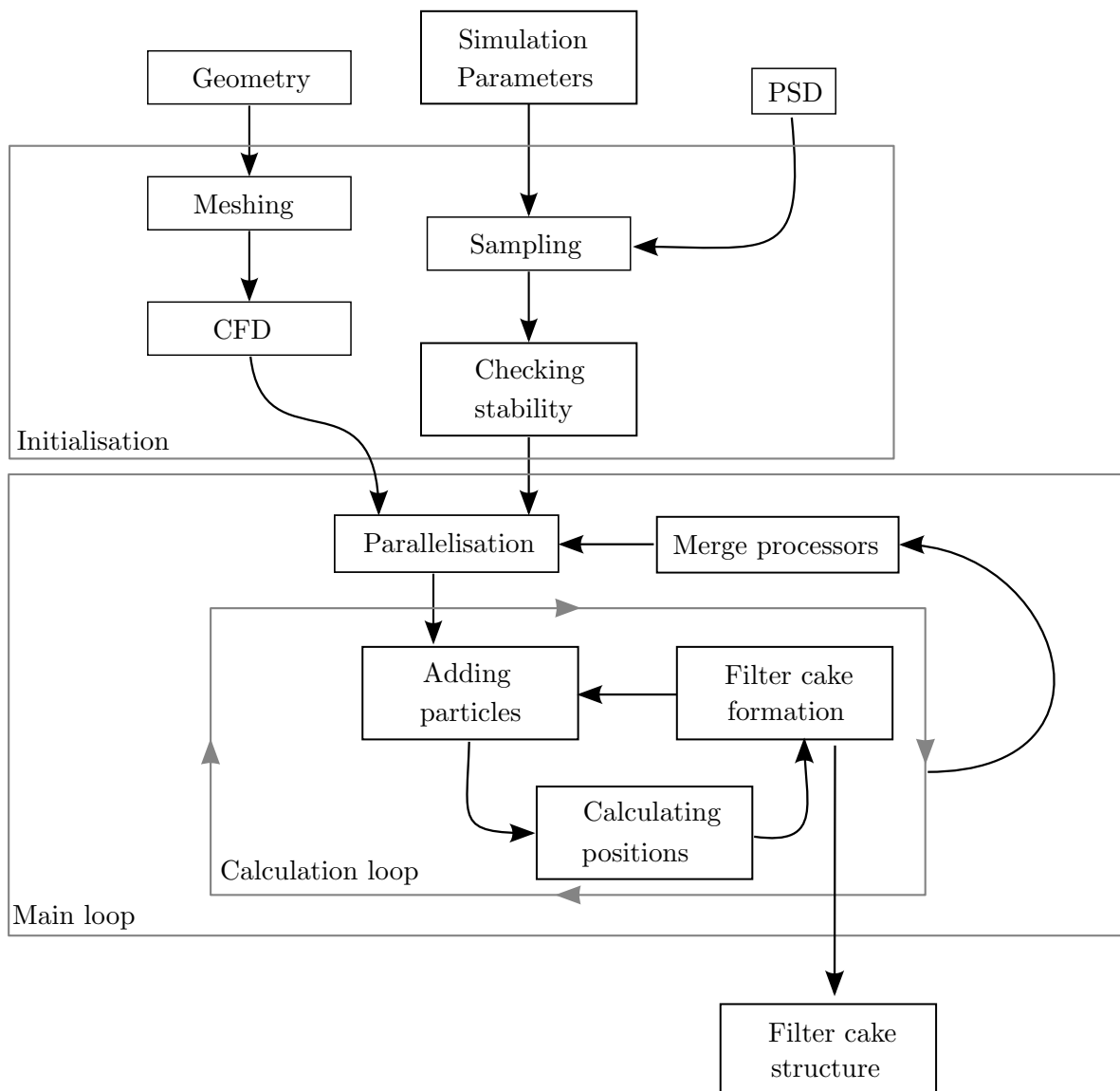


**Figure 4.4:** Overview of the model architecture. The MBR geometry, PSD and the general simulation parameters are the inputs of the model. The output of the model is the filter cake structure, represented by the  $(x, y, z)$ -coordinates and diameter of the particles in the cake.

the first being the MBR geometry. This geometry is defined in a Python script and converted to a suitable mesh by SALOME's Python interpreter. Then, this mesh is exported to OpenFOAM and the solution for the pressure and velocity fields are obtained using the simpleFOAM solver. These fields are subsequently imported to MATLAB. The second input is the PSD of the particle diameters in the feed flow. During the initialisation, the total mass of particles that will flow through the system during the simulation is estimated and sampled as discussed in Section 4.1.1. The last input is a list of general simulation parameters, such as the concentration of particles  $c_b$ , the stickiness parameter  $k$ , the time window considered by the history force, etc. Based on these values, it is first checked if the calculation of the Stokes drag force is stable (Ghijs, 2014). If so, the main loop is entered. If not, an appropriate time step is suggested that leads to stable simulations.

In the main loop, the computational domain is partitioned and assigned to a number of processors (Section 4.3). Each processor carries out a calculation loop to simulate the dispersed phase. Each time step, new particles are added to the system, the new positions of all particles are determined and the filter cake formation is simulated. After a fixed number of time steps, the information of the processors is collected and the domain is repartitioned. This procedure is repeated until the predefined simulation time is reached.

## 4.5 Software

### 4.5.1 MATLAB

MATLAB (v2015a, MathWorks), an abbreviation for matrix laboratory, is a high level matrix-based scripting language licensed by MathWorks. This commercial software package has an extensive library of readily available functions, mostly for engineering and scientific applications (MathWorks, 2016). MATLAB plays a central role in this master thesis, it is the backbone of the model linking all the different processes, software and files and acts as a basis for the GUI.

### 4.5.2 Python

Python (v2.7.3, Python Software Foundation) is an open source, high-level programming language that is more general-purpose than MATLAB. Python is licensed by the Python Software Foundation and comes with a vast number of modules, both from the standard library and community-contributed libraries, making it widely applicable (Python-Software-Foundation, 2016). For this master thesis, Python is mainly used as scripting language for the automated generation of meshes through SALOME's Python interpreter.

### 4.5.3 SALOME

SALOME (v7.6.0, OPEN CASCADE) is an open source software for the pre- and post-processing of numerical simulations. It is used as a pre-processor for the generation of the geometry and mesh before using CFD. SALOME provides an application programming interface (API) for Python that enables scripting of the geometry and mesh, providing a generic workflow for the creation of variable geometries and meshes. SALOME is licensed by OPEN CASCADE (Open-Cascade, 2016).

### 4.5.4 OpenFOAM

OpenFOAM (v2.2.2, OpenFOAM foundation) (Open Source Field Operation and Manipulation) is an open source software package that provides a vast number of solvers and utilities for the calculation of continuum mechanics (OpenFOAM-Foundation, 2016). OpenFOAM is written in C++ and has no GUI, all manipulations are done by changing files and running applications from the command line. Two solvers are used for this master thesis, the simpleFOAM solver is a steady-state solver for turbulent and laminar flow and the pimpleFOAM solver is a large time-step transient solver for turbulent flow.

## 4.6 Post-processing user interface

This advanced mechanistic membrane fouling model aims at identifying the key mechanisms of membrane fouling in filtration processes. In addition to the accurate modelling of membrane fouling, it is important that the simulation results are analysed critically. Therefore, a GUI was developed as post-processing tool that enables, amongst other things, a detailed visualisation of the filter cake and force balance (Figure 4.5). The prominent utilities of this GUI are elaborated below.

By clicking the “*Play*” button [1] the in silico filtration experiment is displayed in real-time speed. With the “*Track*” button [2], one can track individual particles throughout the simulation, while useful information about the particle’s velocity, acceleration, size, etc. is displayed at [2a]. While tracking a particle, the force balance for the two main directions ( $x,y$ ) is shown in two top right plots [2b]. This information is very useful for determining the main driving forces of filter cake formation under various operational conditions. The button “*Detail*” [3] visualises the filter cake at a user-defined position in the form of a two-dimensional projection. The user is able to “scroll” through the filter cake along the length of the membrane for a visual inspection. A three-dimensional visualisation of the filter cake can be requested by clicking “*3D*” [4]. *Diameter coloring* [5] assigns a different color to each particle size which can be convenient for the visualisation of certain phenomena, such as particle size segregation in the cake layer due to preferential sedimentation (Section 5.2.3).

The PSDs of the feed flow, filter cake, dispersed phase and the entire system (control) can be visualised by checking of “*PSD*” [6]. Finally, by clicking “*Save*” [7] all the information of the detailed filter cake is stored in a MATLAB workspace variable for further manipulation outside the GUI.

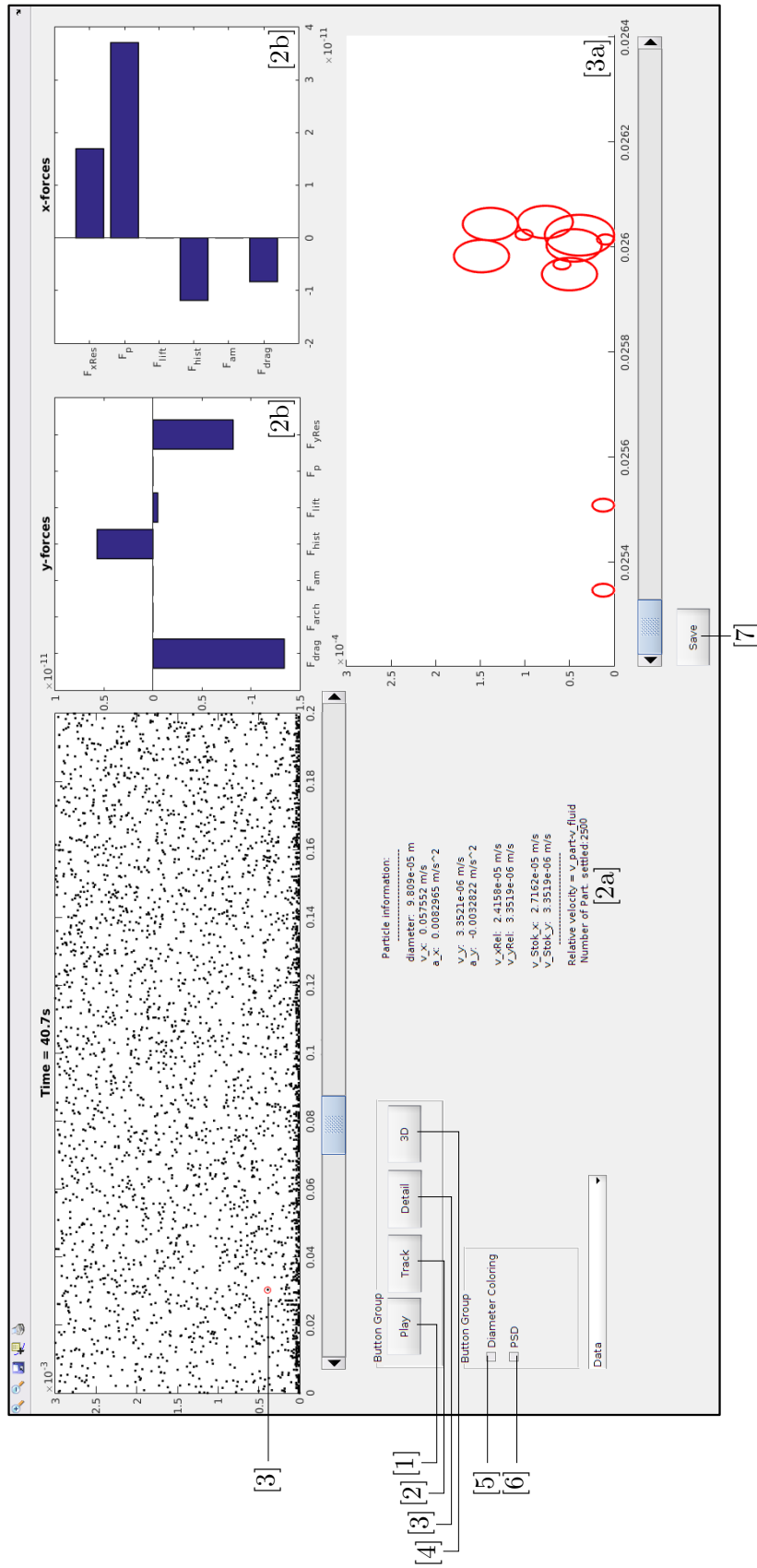


**Figure 4.5:** Graphical user interface for post-processing. Note that the bottom right plot of the filter cake is a two-dimensional projection, there is no overlap of particles.

[7]

# CHAPTER 5

## Results and discussion

One sometimes finds what one is not looking for.

— *Sir Alexander Fleming*

This chapter presents the results of this work and is structured in two major sections. In the first section (5.1), the model-based design of a laboratory scale microfiltration unit is discussed. This unit will be used to collect data for the calibration and validation of the model, and it is of utmost importance that a structured flow is achieved near the membrane. In Section 5.2, a scenario analysis is performed to assess the movement of particles and the filter cake formation under different operational conditions. First, a description of the modelled system and the assumptions are discussed and the benchmark operational parameters are disclosed. Next, a qualitative validation of the bulk phase force balance is performed in order to assess the accuracy of the predicted movement. In the end, the spatial segregation of the particles and the effect of polydispersity is investigated.

### 5.1 Calibration and validation: model-based design of a filtration unit

In order to determine the value of the adhesion parameter  $k$ , which can be interpreted as the stickiness of the filter cake, a calibration has to be performed. Furthermore, as the objective of this research is the characterisation of filter cake formation, it is important to assess the model's accuracy through validation. Both calibration and validation require the acquisition of experimental data. For that reason, a laboratory scale, crossflow microfiltration unit was designed. Such an experimental setup enables full control of the operational conditions and measured quantities during filtration. Moreover, in addition to tracking typical filtration variables such as the transmembrane pressure and flux, it is possible to use profilometric techniques for the acquisition of specific filter cake properties such as the cake thickness, surface roughness and other, more advanced features for a goal-directed calibration/validation.

These filter cake properties are not readily available in literature and can provide valuable insight in filter cake formation.

In order to facilitate the calibration/validation of the model, an experimental filtration unit was designed with CFD that leads to an “ideal” flow behaviour which is postulated in the following three design criteria.

The geometry should, first of all, stimulate laminar flow as turbulence is characterised by unstructured and chaotic flow which, in modelling terms, is a lot harder to describe than the structured laminar flows. Furthermore, it will be a lot easier to unravel the fouling mechanisms taking place in the filtration device, when turbulence effects can be neglected. It is important to keep in mind that this model serves as a proof-of-principle of the physical laws and the scenarios under consideration do not necessarily have to be realistic.

The flow regime is characterised by the ratio of inertial forces to viscous forces, represented by the Reynolds number  $Re [-]$  (Ranade, 2002):

$$Re = \frac{LU_r}{\mu/\rho}, \quad (5.1)$$

with  $L$  [m] the characteristic length. Flow is said to be turbulent for  $Re > 4000$ , laminar for  $Re < 2300$  and transient for  $2300 < Re < 4000$ . The *first design criterion* is thus a laminar flow with a Reynolds number below 800 in the membrane compartment. This conservative Reynolds number is instituted because it is only an indication of the flow regime and not a sufficient criterion, therefore it is to be used with caution. Turbulent flows can further be induced by rough surfaces, inlet phenomena and other processes that are not encompassed by the Reynolds number (Taylor et al., 2006).

The *second design criterion* involves the minimisation of dead volumes within the filtration device. The fluid velocity approaches zero in these regions which will lead to an increased local fouling rate and a smaller effective volume through which there is flow, resulting in higher Reynolds numbers than calculated from Eq. (5.1).

The *third and last design criterion* states that recirculation streams are to be avoided. This criterion is introduced so that a slice of the MBR can be used as the representation of the full system, lowering the computational demands of the model. Such an assumption is not valid when recirculation patterns occur inside the geometry.

For the membrane configuration, a flat sheet membrane was selected for two reasons; the shape of the filtration device for this membrane type is less bound to geometric constraints compared to other membrane configurations and this configuration eases removal of the membrane for profilometric characterisation without perturbing the filter cake. This is much harder (if not impossible) to accomplish with e.g. tubular or spiral wound membranes.

The membrane used in all designs has a width of 10 cm and a length of 30 cm, based on the measurable surface. Figure 5.1 shows a schematic outline of the filtration device and all components. The membrane sheet is positioned on the bottom of the filtration device [2].

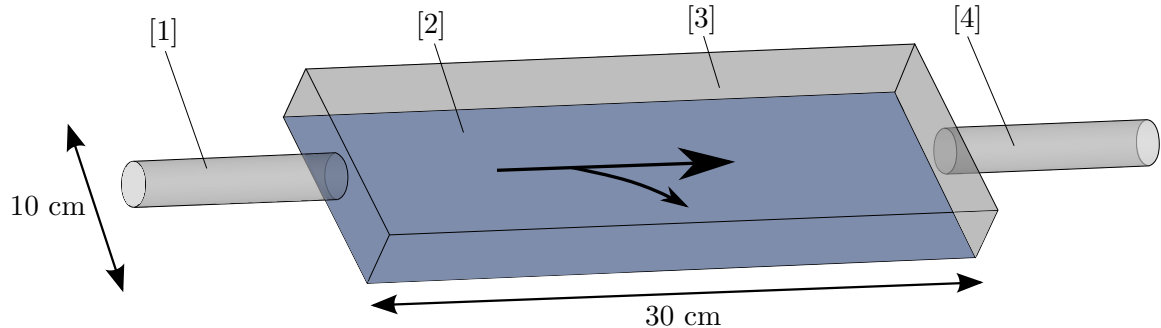


**Figure 5.1:** Schematic representation and dimensions of a potential experimental filtration device with inlet [1], membrane [2], membrane compartment [3] and outlet [4]. The arrow represents the movement of liquid from inlet to outlet and through the membrane.

With the body of the filtration unit established, the effect of different in- and outlet structures was evaluated by means of CFD. Although the flow in the membrane compartment should be laminar due to the chosen crossflow velocity, it is still possible for the inlet to have a turbulent regime. Hence, the turbulent `simpleFOAM` and `pimpleFOAM` solvers were used to obtain accurate results of the internal velocity and pressure fields. The latter were analysed for each design and the in- and outlet structures were modified with targeted adjustments in order to obtain a design that meets all the abovementioned design criteria.

The first inlet structure that was evaluated is a standard cylindrical hose with a diameter of 2 cm. Figures 5.2 (a) and 5.2 (b), respectively, show the three-dimensional overview and the sideview for this geometry, while the fluid streamlines are depicted in Figure 5.3 (a). The streamlines represent the tangent of the velocity field in each point and describe the path of a massless fluid element in the velocity field. This figure clearly shows that such a configuration leads to a considerable recirculation along with the establishment of dead zones in the corners of the membrane compartment. Furthermore, the small cylindrical inlet induces turbulent swirling (which is not visible on figure 5.3 as it is a time dependent phenomenon). In order to avoid recirculation, stagnation and turbulent swirling, the transition from the inlet to the membrane compartment should be more gentle. Therefore, more gradual inlet and outlet geometries were considered.

The next design had a funnel-shaped inlet/outlet structure (Figures 5.2 (c), (d)) and should result in a less aggressive entry of the feed flow. Figure 5.3 (b) indicates that this design has a flow pattern that is less chaotic, while turbulent swirling is absent. However, there is still

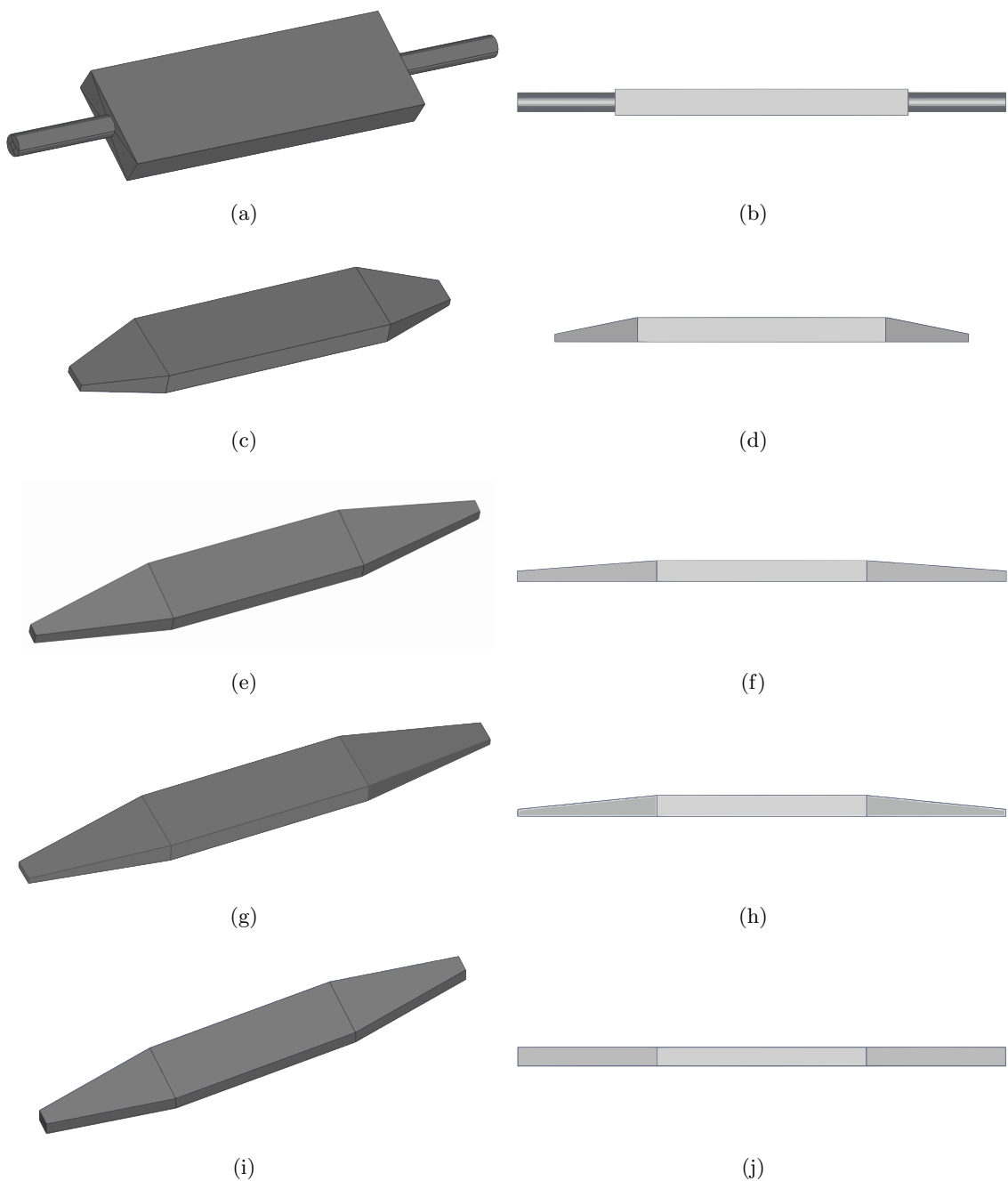


**Figure 5.2:** Tested laboratory scale filtration device geometries with CFD: three-dimensional geometry (left), sideview (right)

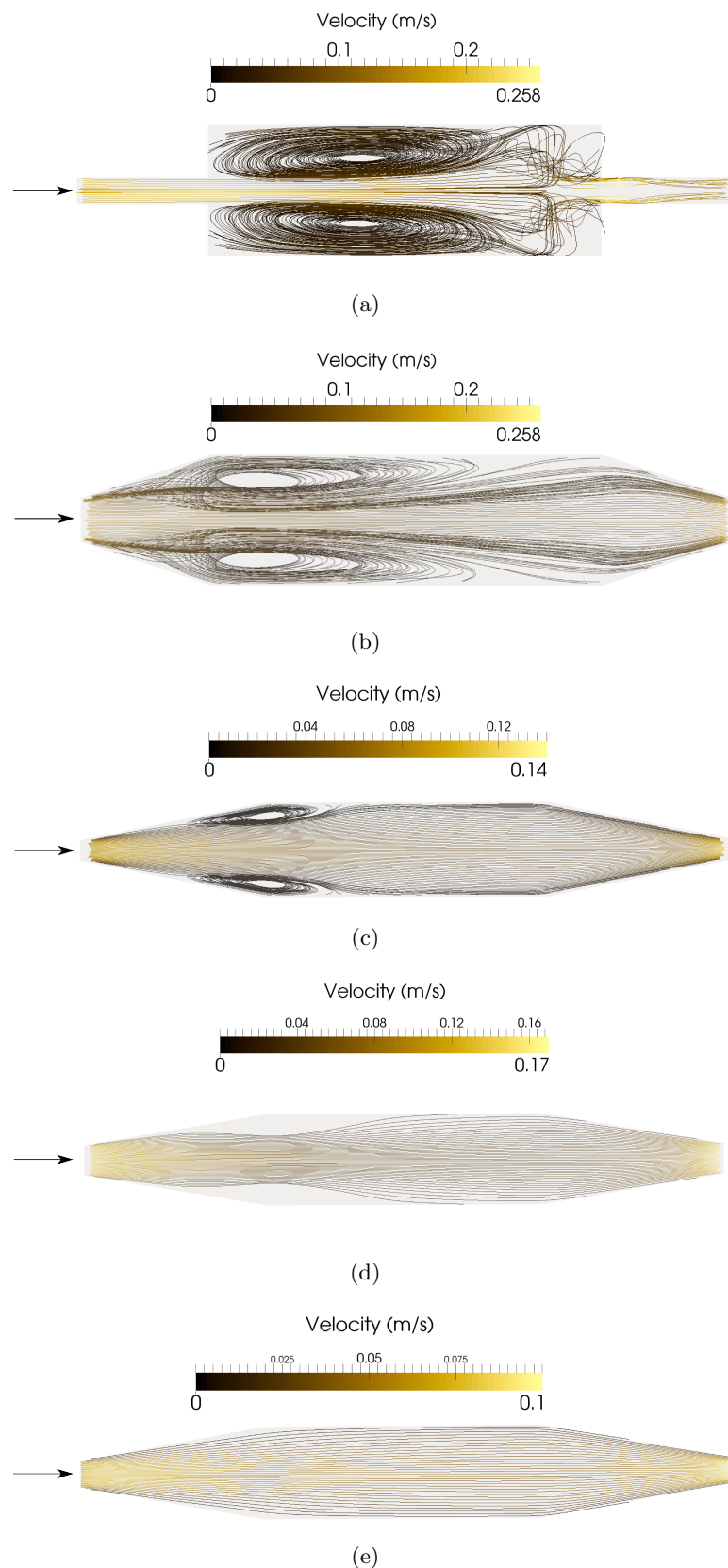


**Figure 5.3:** Velocity and streamlines in the different designs tested in Figure 5.2 (top view). The arrow indicates the inlet of the filtration device.

a considerable recirculation of the fluid and presence of dead volumes. Hence, the feed flow still disturbs the overall fluid dynamics too much.

In an attempt to get rid of the recirculation, the inlet length was doubled from 10 to 20 cm (Figures 5.2 (e), (f)). Figure 5.3 (c) shows the streamlines for this configuration. Although there is a substantial improvement, it still does not meet the requirements set by the design criteria. By using an inlet with a rectangular cross section rather than a square, it is possible to obtain a flow profile without recirculation (Figures 5.2 (g), (h) and Figure 5.3 (d)), but these changes introduce two stagnant regions at the entrance of the membrane compartment. Finally, a suitable design was obtained by introducing a bigger inlet and reducing the height of the membrane compartment so to obtain a flat configuration (Figures 5.2 (i), (j)). This configuration also has the advantage of being a lot easier to manufacture. Since this geometry generates a flow profile that fulfills all design criteria (Figure 5.3 (e)), it will be constructed and used for the experimental measurements. The technical drawings for this design are given in Appendix A.

## 5.2 Filtration model: case studies

### 5.2.1 Setup

In order to investigate the impact of the model extensions and to verify if the filter cake build-up occurs in a realistic way, a tubular membrane was chosen as subject of a scenario analysis. This geometry has the advantage of being symmetrical, it gives rise to a parabolic flow profile and enables the possibility of simulating a long length. Therefore, the tubular geometry was selected instead of the optimal geometry according to the results reported in Section 5.1. The tubular membrane had an inner diameter of 8 mm and a length of 60 cm. The feed was introduced at the channel inlet and a constant flux was instituted through the porous wall (membrane). A crossflow velocity and flux of respectively  $0.04 \text{ m s}^{-1}$  and  $36 \text{ LMH}$  ( $1 \times 10^{-5} \text{ m s}^{-1}$ ) were chosen as benchmark values. The PSD of the feed flow was experimentally determined with a particle size analyser (DIPA 2000) on a sample of MBR sludge from municipal wastewater (Figure 5.4) and the number average diameter,  $40.82 \mu\text{m}$ , was used as benchmark particle size for monodisperse simulations. Ghijs (2014) demonstrated that high values of  $k$  result in a slow filter cake formation while low values induce an increased piling of the particles. Therefore,  $k = 2$  results in a good trade-off between the rate of filter cake formation and the roughness of the cake. The other benchmark parameters are summarised in Table 5.1.

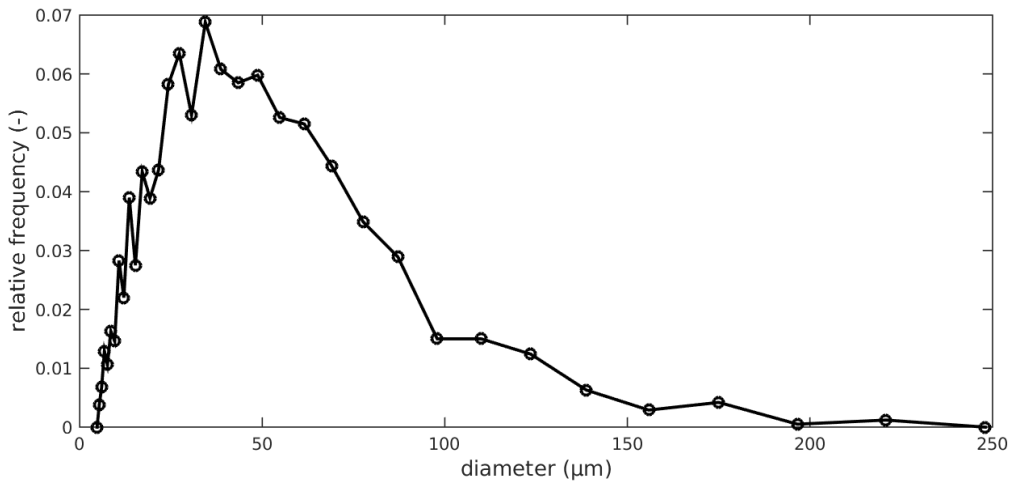


**Figure 5.4:** Experimentally determined particle size distribution of a sample of MBR sludge from municipal wastewater, obtained with particle size analyser (DIPA 2000).

**Table 5.1:** Benchmark parameter values used in the filtration model.

Parameter	Value
$U_{cf}$	crossflow velocity
$J$	flux
$\rho_s$	density of the suspended solids
$\rho_f$	density of the continuous phase
$\nu_f$	kinematic viscosity of the continuous phase
$k$	adhesion parameter
$d_p$	number average particle diameter
$c_b$	concentration of suspended solids

Due to the symmetry of the tubular membrane, it can be represented as a cuboid with a thickness of 0.6 mm (Figure 5.5). Such a representation does not take into account the effects of the curvature. However, this effect is assumed negligible as the height of the cuboid is only 2 % of the cylinder circumference and the fluid dynamics are consequently computed in two dimensions.

In order to simulate the flow fields in OpenFOAM, a mesh was generated with a resolution of 0.6 cm in the  $x$ -direction and 0.04 mm in the  $y$ -direction, resulting in a  $300 \times 100$  mesh with 30,000 cells. Next, the boundary faces were defined on the mesh and the boundary conditions were imposed. The inlet and membrane face were defined as the patch-type which is able to account for a flux. Dirichlet boundary conditions were imposed of  $0.04 \text{ m s}^{-1}$  for

the  $x$ -velocity at the inlet,  $1 \times 10^{-5} \text{ m s}^{-1}$  for the  $y$ -velocity at the membrane and  $0 \text{ m s}^{-1}$  for all other directions, assuming zero slip at the walls. For the pressure, Neumann zero gradient boundary conditions were set at the inlet, membrane, and symmetry plane. The outlet was also defined as the `patch`-type with a zero gradient Neumann boundary condition for the velocity and a Dirichlet boundary condition of atmospheric pressure, assuming free outflow. The inside face was defined as a `symmetryPlane`-boundary implying a periodic boundary condition for the velocity, while the front and back faces are set to `empty` to indicate a two dimensions simulation. The Reynolds number for these conditions is 320, which is well within the laminar region.

The steady-state solution for this flow problem was obtained via the `simpleFoam` solver which is primarily used for turbulent, incompressible Newtonian flow but is also valid under laminar conditions.

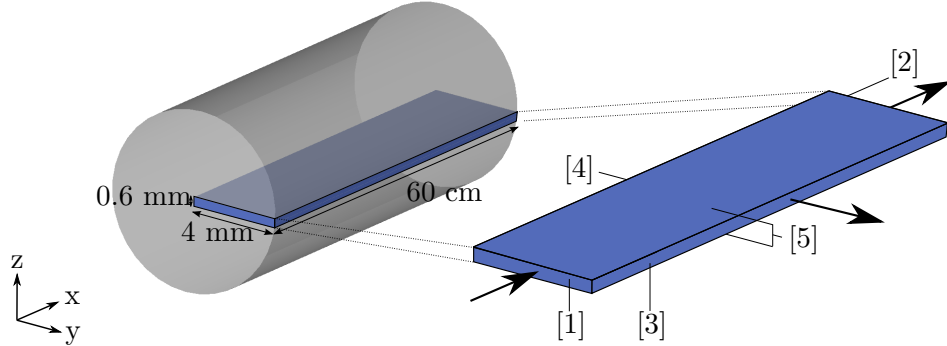


**Figure 5.5:** Three-dimensional representation of the modelled system, boundary faces and their respective fluxes, denoted by the arrows. The boundary faces consist of inlet [1], outlet [2], membrane [3], inside [4], front and back [5].

The steady-state solution for the relative kinematic pressure  $\psi [\text{m}^2 \text{s}^{-2}]$ ,  $x$ -velocity and  $y$ -velocity is displayed in Figure 5.6. The absolute pressure shows a linear decrease from 101,371 Pa to atmospheric pressure, 101,325 Pa. Concerning the fluid velocity, a transition from the uniform profile at the inlet to a parabolic profile is observed. Due to the zero-slip boundary condition at the membrane, the fluid is moving slower near the walls and the incoming fluid is forced towards the middle section. After this transition, the  $x$ -velocity exhibits a fully developed parabolic flow and the  $y$ -velocity remains quasi constant at  $-1 \times 10^{-5} \text{ m s}^{-1}$ . In order to facilitate the interpretation of the results, all simulations performed in the remainder of this chapter are based on the fully developed middle section of the tubular membrane (30 cm). The involvement of inlet phenomena will only complicate the interpretation and are removed from the equation. Lastly, it is important to note that all simulations employ the benchmark parameter values as given in Table 5.1, unless indicated otherwise.

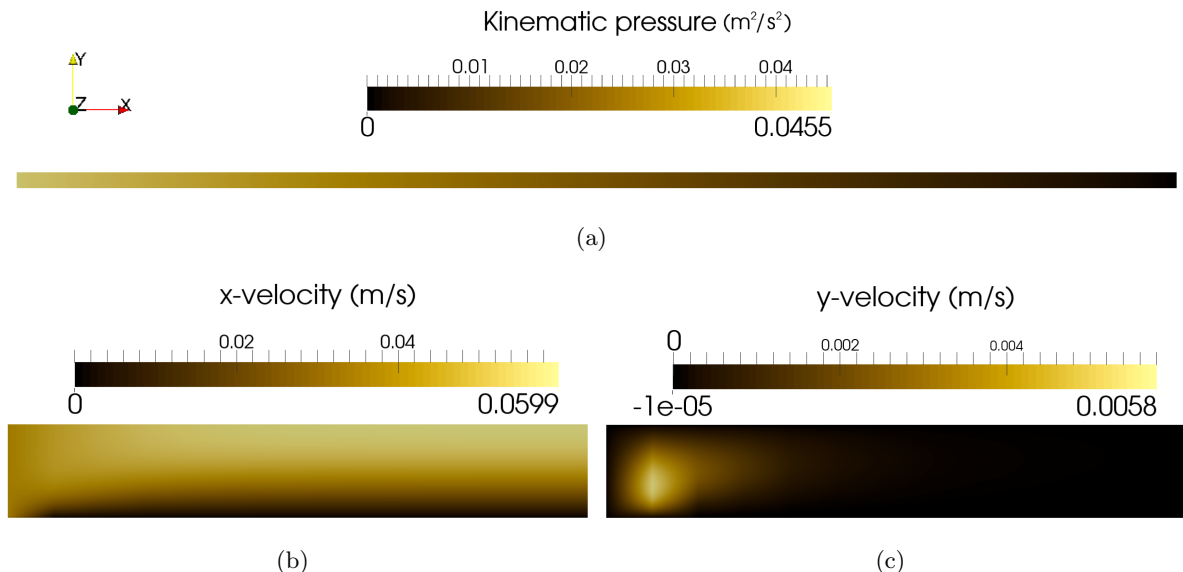


**Figure 5.6:** (a) Relative kinematic pressure field in the slice of the tubular membrane (60 cm). (b)  $x$ -velocity in the first 2.5 cm of the modelled system. (c)  $y$ -velocity in the first 2.5 cm of the modelled system.

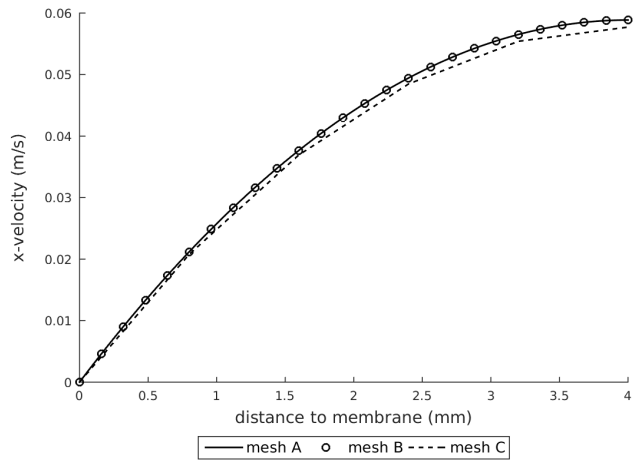
### 5.2.2 Mesh independence of the continuous phase

The mesh size is a critical factor that defines the accuracy of the CFD simulations. In order to achieve accurate results, the mesh size should be sufficiently fine. However, the accuracy increases asymptotically and there is a refinement level beyond which there is no further significant effect of the mesh size. At that level, mesh independency is attained (Roache, 1997), which is to be pursued.

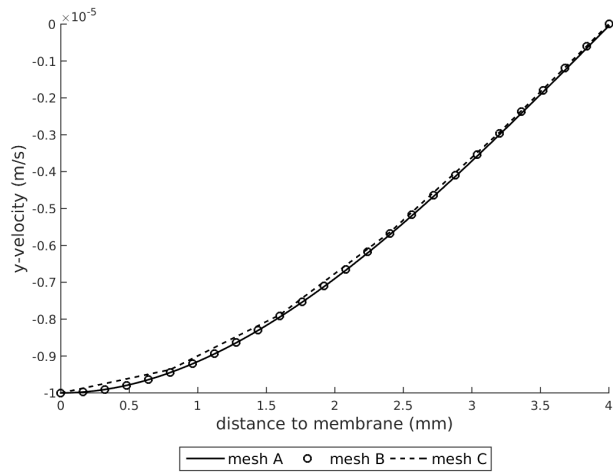
To determine the independency of the mesh, three meshes of different sizes were constructed; Mesh A had a cell size of 20 mm by 40  $\mu\text{m}$ , mesh B a cell size of 60 mm by 200  $\mu\text{m}$  and mesh C a cell size of 60 mm by 400  $\mu\text{m}$ . These meshes were expected to cover a good range in order to indicate mesh independency. The  $x$ - and  $y$ -velocity were subsequently analysed for several cross sections along the length of the tube. The velocity profiles at  $x = 15 \text{ cm}$  are shown in Figure 5.7.

It can be seen that the velocity profiles of mesh A and B are close to identical whereas a considerable difference is noticeable for mesh C. As a result, one can conclude that mesh A attains great accuracy, but is too fine and hence computationally inefficient, while mesh C is too coarse, giving rise to inaccurate results. Therefore, mesh B provides the best trade-off between accuracy and speed and is the ideal mesh size for the geometry at hand. Figure 5.7 also indicates that the discrepancies increase with the velocity magnitude, making it possible to use a coarser mesh in low velocity regions. However, due to the imposed flux at the membrane, the regions with a low  $x$ -velocity are also the regions with a high  $y$ -velocity.

Hence, a non-uniform mesh should be a fine mesh near the membrane, a coarser mesh in the middle and finer mesh at the center of the tube. Due to the simple geometry and the fast convergence for mesh B, this non-uniform meshing strategy is considered as too complex for a minor efficiency gain, and was therefore not implemented.



(a)



(b)

**Figure 5.7:** Velocity profile of the velocities in  $x$ -direction (a) and  $y$ -direction (b) at  $x = 15$  cm from the inlet for three meshgrids. Mesh A with a cell size of 20 mm by 40  $\mu\text{m}$ , mesh B with a cell size of 60 mm by 200  $\mu\text{m}$  and mesh C with a cell size of 60 mm by 400  $\mu\text{m}$ .

### 5.2.3 The Segré-Silberberg effect: a qualitative validation

Rigid spheres flowing in tubular channels under laminar conditions are subjected to a radial migration due to shear gradient and inertia-induced lift forces. This effect is called the Segré-Silberberg effect and was experimentally observed by Segré and Silberberg (1961). Following the work of Segré and Silberberg (1961), Matas et al. (2004) formulated a theoretical underpinning for this effect, which can be summarised as follows;

Neutrally buoyant particles, which are assumed to move at the speed of the surrounding fluid, are subjected to a lift force away from the channel's center axis when flowing in a channel due to the curvature of the Poiseuille flow . This force is counteracted by wall repulsion effects due to the asymmetric wake of the particles near the wall, inducing a lift force in the opposite direction (Zeng et al., 2005). For low Reynolds numbers, an equilibrium position is reached at approximately 60 % of the distance from the center axis to the wall.

Non-neutrally buoyant particles, which are assumed to lead or lag the surrounding fluid velocity, are additionally affected by the Saffman lift force, Eq. (4.7), and the equilibrium position is not fixed but depends on the size of the channel, the Reynolds number (Eq. (5.1)) and the particle Reynolds number  $Re_p$ :

$$Re_p = \frac{\mathbf{U}_m d_p}{\nu_f D_h}, \quad (5.2)$$

with  $\mathbf{U}_m$  [ $m s^{-1}$ ] the maximal channel velocity and  $D_h$  [m] the hydraulic diameter (Segré and Silberberg, 1961; Matas et al., 2004).

High Reynolds numbers indicate a flow regime that is governed by inertial forces. Saffman's lift force is one of these forces, so it is not surprising that high Reynolds flows result in a more pronounced radial migration of dispersed particles. The same reasoning is valid for the particle Reynolds number (Di Carlo et al., 2007).

The theoretically and experimentally acknowledged Segré-Silberberg effect provides an ideal opportunity for a qualitative validation of the force balance. By means of a series of in silico experiments, an attempt was made to replicate this effect and study its dependency on both Reynolds numbers. As a full analysis of the effect of all variables in Eq. (5.1) and (5.2) is not feasible within the context of this master thesis, only the effect of the particle diameter  $d_p$  and the crossflow velocity  $\mathbf{U}_{cf}$  was investigated. It should be noted that the particle diameter only affects  $Re_p$  while the crossflow velocity impacts both  $Re$  and  $Re_p$  (Eqs. (5.1) and (5.2)).

#### Setup

For this validation, the tubular setup was used from Section 5.2.1. No flux was imposed at the membrane and an infinitely long tube was simulated by employing periodic boundary conditions at the inlet and outlet of the modelled system (Figure 5.5). Figure 5.6 demonstrates

that this periodic boundary condition does not impose a problem for the  $x$ - and  $y$ -velocity as they are constant with respect to the  $x$ -direction in the fully developed middle section of the tubular membrane (30 cm). The same conclusion is valid for the pressure, even though it is not constant, because only the gradient is considered by the force balance, which is also constant with respect to  $x$ . For the initial condition, particles were inserted at fixed points at the inlet and their  $y$ -position is followed in time.

### Effect of the particle diameter

First, the effect of the particle diameter is investigated. Particles of 25  $\mu\text{m}$ , 70  $\mu\text{m}$  and 100  $\mu\text{m}$  were introduced at the inlet, every 0.5 mm and their lateral position was tracked for 120 s. The results of this simulation are displayed in Figure 5.8 (a).

It is clear that there is a clear correlation between the particle size and the radial migration in the high-shear regions of the channel, i.e. close to the membrane. This non-linear effect can directly be accounted to the inertial lift force (Eq. (4.7)), which is quadratic with respect to  $d_p$ . The smallest particles (25  $\mu\text{m}$ ) are almost unaffected by the radial migration.

As mentioned previously, the particles should theoretically reach an equilibrium position between the membrane and the center axis of the tube. This equilibrium position is not observed in Figure 5.8, but this is further discussed in Section 6.1.

### Effect of the crossflow velocity

Next, the effect of the crossflow velocity is examined. The setup was identical to the previous scenario but only one particle diameter i.e. 70  $\mu\text{m}$  was explored. Figure 5.8 (b) depicts the results of this scenario. It can be seen that higher crossflow velocities bring forth an increased radial migration, just as predicted by Matas et al. (2004). This effect demonstrates that particles are more likely to reach the membrane at high crossflow velocities. This observation is interesting as it is generally accepted that such conditions give rise to less filter cake formation by an increased detachment. This exemplifies the complexity of this process and indicates the need for an accurate calibration of the adhesion parameter  $k$ . In the long run, it would be meaningful to implement a more mechanistic approach like a force balance on filter cake particles (Section 6.2).

### Effect of the flux

Since the effect of a radial flux is not included in the Segré-Silberberg effect, it should be investigated how this affects the previous described balance of forces. To investigate this, the particle streamlines were evaluated for a flux of 0 LMH, 36 LMH and 72 LMH, the last two are typical values for membrane filtration. The results of this in silico experiment are presented in Figure 5.8 (c). It can be seen that the flux is the most important factor impacting the radial migration of suspended solids. When applying a flux, smaller particles which are less

influenced by the radial migration effects, are also transported towards the membrane surface. Under these conditions the non-existence of an equilibrium position seems to be justified.

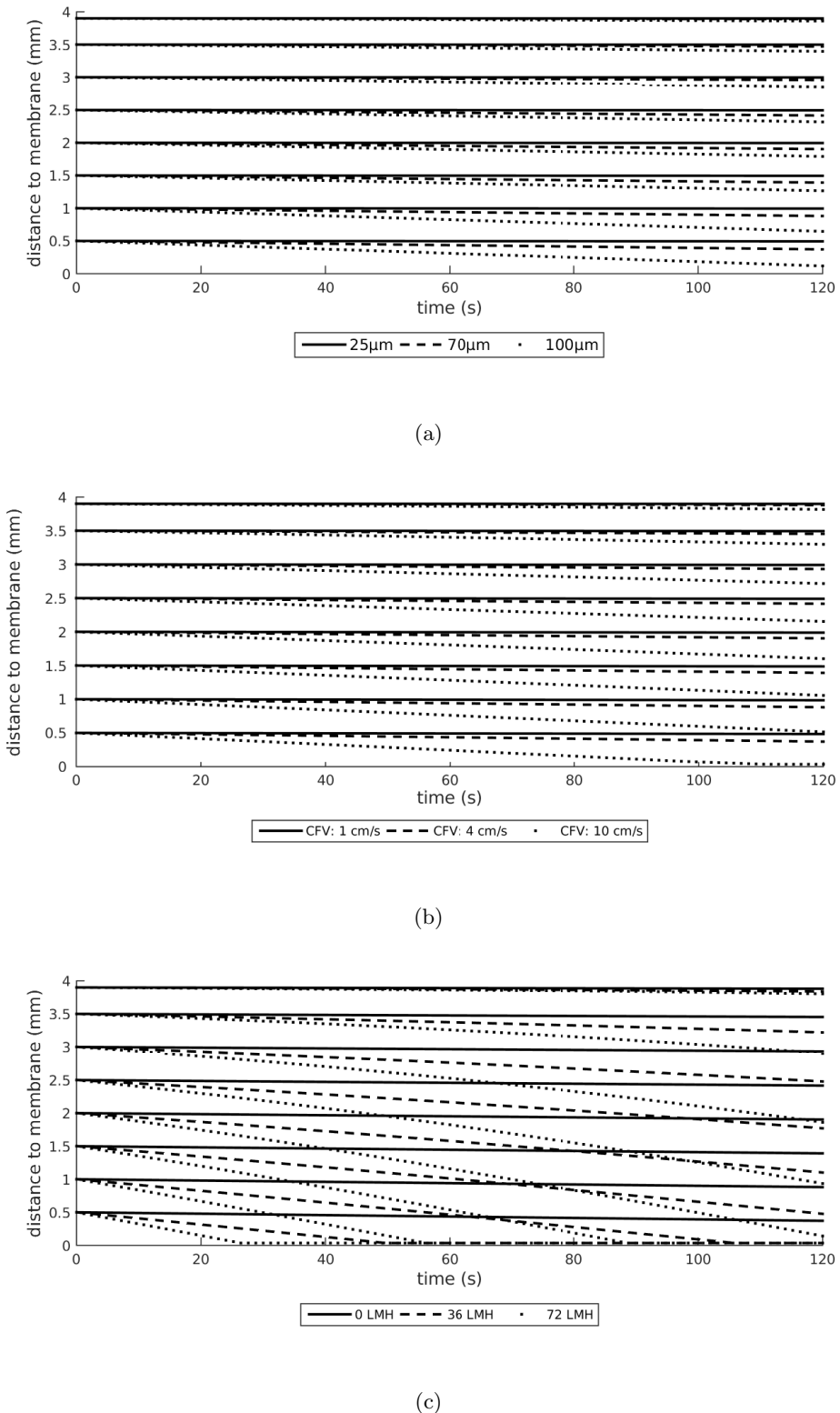


**Figure 5.8:** Effect of the particle diameter (a), crossflow velocity (b) and transmembrane flux on the radial migration of particles in a microchannel.

### 5.2.4 Mesh independency of the agent-based model

Checking the mesh independence is good modelling practice for CFD and since the Lagrangian modelling framework relies on the pressure and velocity field generated by CFD, it seems only logical to perform a mesh independency check on the ABM as well. This might provide information about the sensitivity towards variations in the flow field. The particle streamlines are simulated for the same mesh sizes as the mesh independency in Section 5.2.2.

From Figure 5.9 it is clear that the movement of the particles shows the same sensitivity towards the mesh size as the velocity profiles, which is expected as some forces are directly proportional to the velocity. The regions with the largest deviation of the streamlines are related to the regions with the largest deviation of the velocity profile, i.e. at high  $x$ -velocities. For particles introduced near the center axis of the tube, the radial lift force is almost zero and, hence, these are in an unstable equilibrium position. Therefore, the particle tracers at  $y = 3.9$  mm are not significantly impacted by the mesh size.

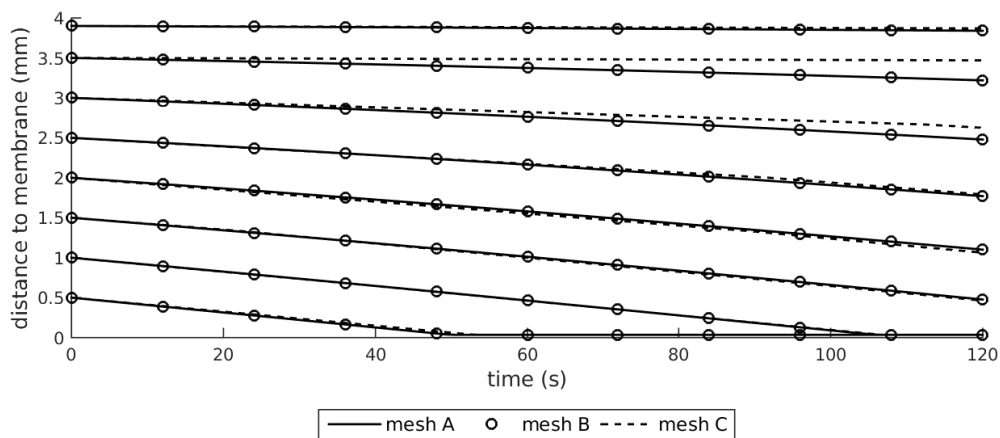


**Figure 5.9:** Effect of the mesh size on the particle streamlines in a tubular membrane filter.

### 5.2.5 Spatial segregation of the suspended particles

The dependency of the radial migration velocity on the particle size, demonstrated in Section 5.2.3, should lead to the segregation of deposited particles along the longitudinal axis of the membrane. This effect will be most noticeable for an adhesion probability of 100%, as it eliminates the stochasticity of the filter cake formation. Hence, perfect stickiness of the particles was assumed for this simulation, to demonstrate the segregation. Particles were introduced in the lower 1 mm of the inlet and the deposition position of the particles was tracked. A normalisation of the number of deposited particles at each bin with respect to the

total number of deposited particles gives rise to a histogram as depicted in Figure 5.10. A flux and crossflow velocity of respectively 144 LMH and  $10 \text{ cm s}^{-1}$  were employed and the dispersed phase consisted of number-wise equally represented particle sizes of 40, 70 and 100  $\mu\text{m}$ . It was chosen to only consider the lower mm in order for all entering particles to deposit within a reasonable time frame. The same reasoning can be used to motivate the choice of a higher flux and crossflow velocity as it brings forth a faster radial migration.

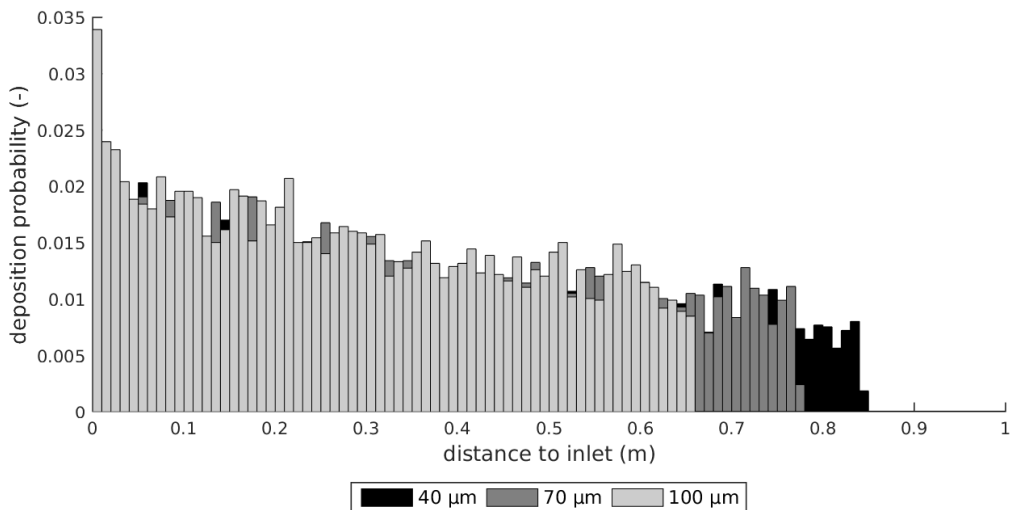


**Figure 5.10:** Relative frequency of the number of deposited particles in function of the distance to the inlet for particles of 40, 70 and 100  $\mu\text{m}$ .

Figure 5.10 shows that there is indeed a longitudinal segregation of the suspended solids. The largest particles deposit closer to the inlet than the smaller particles. There is a clear cut-off distance for each particle size which is the deposition position of the particles that are introduced at the top of the inlet. As a consequence, all particles deposit within this distance. It is also clearly visible that the number of depositions decreases with the distance, which can be explained by the fact that, close to the membrane, a small difference in inlet position induces only a small difference in the particle trajectory due to the low velocity of the continuous phase. For higher fluid velocities closer to the middle of the tube a small change in the entry position results in a big difference in the trajectory.

It should be kept in mind that an adhesion probability of 100% is not realistic but the purpose of this experiment was to characterise the movement of the suspended particles and not the simulation of a realistic filter cake build up.

### 5.2.6 Effect of polydispersity

In order to assess the effect of polydispersity, a comparison was made between the filter cake of a mono- and polydisperse bulk phase. This is also the ideal opportunity to perform a full-fledged simulation with filter cake formation to identify the model imperfections.

The polydisperse simulation used an experimentally determined PSD of MBR sludge (Figure 5.4) and the monodisperse simulation used the number average particle size of this distribution, which was  $40.82\text{ }\mu\text{m}$ . The filter cake formation was simulated for 15 s and each scenario was run four times in order to assess the stochastic nature of the model, which is depicted as a band (average, minimum and maximum) in Figure 5.11. The average filter cake thickness in time is presented in Figure 5.11 (a) and shows that polydispersity gives rise to a faster filter cake build up. Section 5.2.5 demonstrates the fast deposition of big particles and, in a polydisperse setting, these will “catch” smaller particles giving rise to a fast filter cake development. This synergistic effect is not present in a monodisperse setting and the filter cake is thereby formed at a slower pace. The evolution of the filter cake porosity is shown in Figure 5.11 (b). Initially, there is no filter cake and the porosity is equal to one, and due to the formation of filter cake patches the porosity starts decreasing at a higher rate in the polydisperse setting. This could, however, be due to a denser filter cake or a higher surface coverage, which cannot be determined from the figure. For this, the porosity of the actual filter cake patches has to be evaluated (Figure 5.11 (c)). It can be seen that the filter cake in the polydisperse setting is more densely packed than in the monodisperse case. As mentioned previously, polydispersity should theoretically lead to a denser packing of the particles in the filter cake. Hence, the simulation results are in agreement with the literature (Desmond and Weeks, 2014; Sohn and Moreland, 1968).

However, these simulation results still have their imperfections. Figure 5.12 shows a two-dimensional projection of the centers of the deposited particles after 2 min of simulation (the monodisperse case). Note the unrealistic architecture of the filter cake, embodied by the formation of narrow filter cake piles. This observation is confirmed by the longitudinal variance of the filter cake thickness, presented in Figure 5.11 (d). Hence, it can be concluded that the problem of particles piling up was not resolved by transitioning to a three-dimensional model.

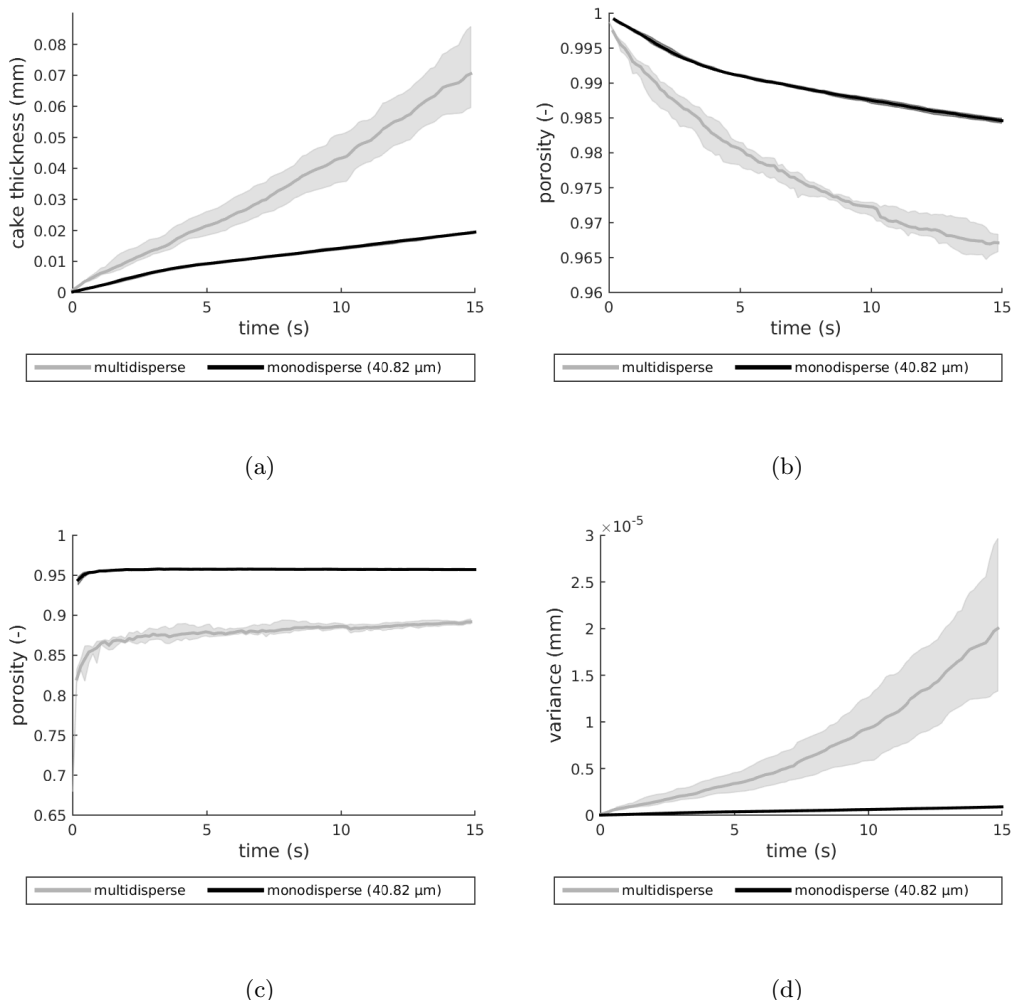


**Figure 5.11:** Evolution of the simulated filter cake characteristics in time. (a) Average filter cake thickness, (b) global filter cake porosity, (c) actual filter cake porosity, (d) longitudinal variance of the filter cake thickness.

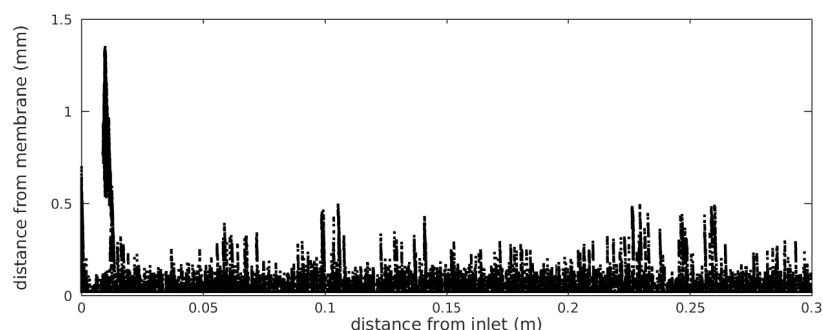


**Figure 5.12:** Two dimensional projection of the filter cake after 2 min. The dots represent particle centers and are not to scale with the particle size.

# CHAPTER 6

## General discussion and perspectives

Despite of the accomplished progress, the model still has a few shortcomings and it is important to address these. Besides, looking forward, guidelines and remarks are provided for future improvements. In the final part of this chapter, different sources of numerical instability are mapped out and a brief discussion on the suitability of different profilometric techniques for the specific task of characterising the filter cake is given.

### 6.1 Remarks on the bulk phase force balance

In Chapter 5, a qualitative validation is performed of the force balance in the model. The results were mostly in agreement with the theoretical description of Matas et al. (2004) and the experimental observations of Segré and Silberberg (1962) and Di Carlo et al. (2007). Still, the absence of an equilibrium position raises questions about the integrity of the force balance (Eq. (3.3)). The reason for this apparent shortcoming should be sought in the forces that are able to counteract the radial migration of particles. Zeng et al. (2005) indicate that the presence of a nearby wall breaks the axisymmetry of the wake vorticity distribution as well as a tortuosity change, inducing a lift force that moves the particles away from the wall. This mechanism is not explicitly included in the force balance but might be accounted for under the guise of the Faxén correction:

$$\mathbf{U}_{r,\text{eff}} = \mathbf{U}_r - \frac{1}{24} d_p^2 \nabla^2 \mathbf{U}_c, \quad (6.1)$$

with  $\mathbf{U}_{r,\text{eff}}$  [ $\text{m s}^{-1}$ ] the Faxén corrected relative velocity and  $\mathbf{U}_r$  the actual relative velocity of the particles. In two dimensions, the Laplacian of Eq. (6.1) can be written as,

$$\nabla^2 \mathbf{U}_c = \frac{\delta^2 \mathbf{U}_c}{\delta x^2} + \frac{\delta^2 \mathbf{U}_c}{\delta y^2}. \quad (6.2)$$

A fully developed Poiseuille (parabolic) flow is assumed in the tube. For this flow regime, the second derivative of  $\mathbf{U}_c$  with respect to  $y$  is constant along the width of the tube. Hence,

$$\frac{\delta^2 \mathbf{U}_c}{\delta y^2} = c. \quad (6.3)$$

Furthermore,  $\mathbf{U}_c$  is constant with respect to  $x$  under these conditions, so

$$\frac{\delta^2 \mathbf{U}_c}{\delta x^2} = 0. \quad (6.4)$$

Therefore,

$$\frac{1}{24} d_p^2 \nabla^2 \mathbf{U}_c = c, \quad (6.5)$$

and this shows that the Faxén correction is constant for a Poiseuille flow and is clearly not the wall repulsion effect described by Zeng et al. (2005), which reaches a maximum magnitude near the walls.

In order to increase the accuracy of the force balance, it might be interesting to investigate the addition of the wall-induced lift force as it seems to have a considerable impact on the flow of particles. Furthermore, next to Saffman's lift force, two additional lift forces are described in Matas et al. (2004); the shear gradient-induced lift force due to the curvature of the velocity profile and the Magnus effect due to the forced rotation of the particles. It is likely that the Magnus effect is negligible compared to the inertial lift force, but the shear gradient-induced lift force might be of the same order of magnitude, and should therefore be investigated.

Due to the uncertainty of the magnitude of these forces and the complex nature of their interaction with other operational variables, it is meaningful to first validate the model in order to assess the necessity of an extension of the force balance.

## 6.2 Filter cake formation

The simulation results in Section 5.2.6 indicate the formation of filter cake towers, in spite of the extension of the model to three dimensions. In order to resolve this unrealistic behavior, a rolling algorithm should be included in the model. This will assure that only particles that reach a stable position will attach to the filter cake. As mentioned previously, such a framework is described in Cao et al. (2015) and should be assigned a high priority in the further development of the model as it is imperative for the simulation of realistic filter cake structures.

Next to the packing of particles, it is meaningful to reflect on the adhesion probability equation (Eq. (3.5)). Although this equation serves its purpose of constraining the filter cake formation to low shear regions quite well, several arguments indicate the necessity for the revision of this equation. Firstly, due to the stochastic nature of the model, there is always a chance that particles adhere in high shear regions, and currently these particles remain

attached indefinitely. Secondly, the simulations indicate a positive correlation of the radial migration magnitude and the particle size, resulting in an easier filter cake formation for bigger particles. This contradicts the experimental observations in Li et al. (1998). Hence, it seems that Eq. (3.5) is not able to accurately simulate the balance between adhesion and detachment of particles to the membrane or filter cake, which is a complex interplay between particle-particle interactions (attachment to the filter cake), particle-interface interactions (attachment to the membrane) and the liquid flow (shear at the membrane, compression due to TMP, etc.). A theoretical foundation for particle-particle and particle-interface interactions in dispersions is provided by the Derjaguin, Landau, Verwey and Overbeek (DLVO) theory, which determines the balance between the electrostatic repulsion and the van der Waals attraction (Lyklema, 1968). However, the DLVO theory does not comprise all the necessary processes for a complete representation of the interactions. The agglomeration of particles is also influenced by hydration forces, steric forces and hydrophobic interactions (Van Oss, 1989; Hermansson, 1999). Finally, the hydrodynamics and pressure-driven effects should also be accounted for as it is hypothesised that these effects greatly influence the formation of the filter cake. It can be concluded that Eq. (3.5) is too simple for an accurate representation of filter cake formation and it is clear why it does not yield satisfactory filter cake structures. Moreover, a mechanistic approach in the form of a force balance over the particles in the filter cake is imperative in order to simulate and comprehend backwashing and aeration processes.

### 6.3 Coupling ABM and continuous model

As mentioned in Chapter 3, the two model layers are coupled unidirectionally. The steady-state flow profile of the continuous phase is calculated once at the beginning of the simulation and is used throughout the whole simulation. Hence, the formation of the filter cake has no impact on the continuous phase and the permeate keeps flowing unperturbed, regardless of the fouling severity, which is not at all realistic. Two effects can be identified that demonstrate the impact of filter cake on the surrounding fluid.

The first is the effect of the filter cake by increasing the filtration resistance. An increase in filtration resistance due the presence of a porous filter cake in a certain region will make the fluid move towards cleaner regions, which implies the spatial variation of the flux. Additionally, the presence of a filter cake has an effect on the velocity of the surrounding fluid. Here, it is not the flux that is affected, but rather the general flow profile. Both effects are currently not included in the model but with for a realistic filter cake formation model, at least the increasing filtration resistance should be considered.

To model this, a RIS approach can be applied with two resistance terms, the clean membrane resistance ( $R_m$ ) and the filter cake resistance ( $R_c$ ):

$$R_{\text{tot}} = R_m + R_c , \quad (6.6)$$

where  $R_c$  can be obtained from:

$$R_c = l K_c, \quad (6.7)$$

and  $K_c$  is obtained from:

$$K_c = \frac{K 90}{\bar{d}_p} \frac{(\epsilon)^2}{(1 - \epsilon)^3}. \quad (6.8)$$

where  $K_c$  [ $\text{m}^{-2}$ ] is the specific cake resistance,  $l$  [m] the filter cake thickness,  $K$  [-] the kozeny constant,  $\bar{d}_p$  [m] the mean particle diameter and  $\epsilon$  [-] the filter cake porosity.

By plugging the total filtration resistance  $R_{\text{tot}}$  into Darcy's law, an expression is obtained to calculate the flux:

$$J = \frac{\Delta p}{R_{\text{tot}} \nu_f}, \quad (6.9)$$

The flux decrease could be considered homogeneously over the entire membrane. However, the creation of a realistic filter cake architecture requires a spatially variable flux. So, a sectional approach similar to Li and Wang (2006) should be used (Figure 6.1). Hence, the membrane surface is subdivided in sections with a constant length ( $\Delta x$ ). The flux through each section is calculated with Eqs. (6.6)-(6.9). The newly calculated fluxes are subsequently employed as boundary conditions on the membrane face and a new flow profile has to be generated via CFD.

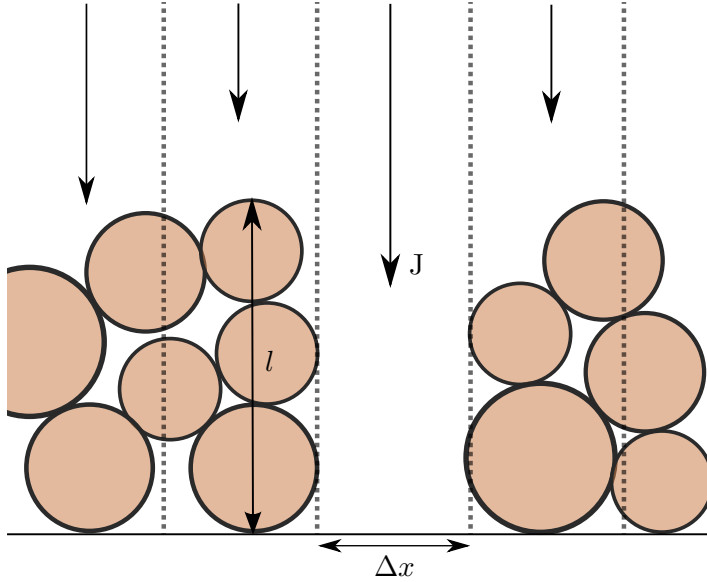


**Figure 6.1:** Schematic representation of a heterogeneously distributed flux along the membrane surface.

In order to account for the variable flux, a bidirectional coupling has to be established between CFD and the ABM, which is, however, not straightforward because both model layers are implemented in different software platforms. Nonetheless, two approaches are identified to establish such a coupling.

The first approach involves using a third program as a wrapper that distributes the flux data from MATLAB to OpenFOAM and the flow profile from OpenFOAM to MATLAB. This approach is the most straightforward and can be accomplished by means of shell scripting. The second approach involves setting up a MATLAB engine script in OpenFOAM that compiles MATLAB's m-code to C++. This approach is much more complex, but is computationally very efficient.

In order to be able to account for the direct effects of the filter cake on the surrounding liquid, it is necessary to explicitly model the suspended particles and the interactions with the continuous phase. This can only be achieved with discrete element methods.

## 6.4 Sources of numerical instability

It is important to keep in mind that this spatio-temporal model basically consists of a system of PDEs which are discretised and solved numerically. These methods can suffer from numerical instabilities and this is also the case for this model. As it seems important for future work, a brief overview is provided of the causes of numerical instability.

The first source of instability is described in Ghijs (2014) and concerns the Stokes drag force which introduces a maximum solver time step limited by the smallest particle diameter, i.e.

$$\Delta t \leq \frac{\rho_p d_p^2}{18 \nu_f}. \quad (6.10)$$

A second source of instability are the velocity fields from CFD. The convergence criteria of the OpenFOAM solvers are set to  $10^{-7}$  which means that openFOAM will stop iterating when the difference between the fields of the current and previous iteration is smaller than  $10^{-7}$ . This results in velocity fields where zeros are actually numbers between  $10^{-8}$  and  $-10^{-8}$ . Although seemingly unimportant, this causes numerical instabilities due to the sensitivity of the force balance to the sign of the fluid velocity. This issue can be easily solved by employing a filter on the velocity values setting all values below the convergence criteria to zero.

Lastly, an additional constraint on the solver time step was found, this time originating for large particles ( $d_p > 100 \mu\text{m}$ ) in the system. Under high crossflow velocities and fluxes, the radial migration of particles is a lot more prominent and forms another source of numerical instability. Nevertheless, it is likely that for more extreme conditions this instability will also impact smaller particles and it should be further investigated.

## 6.5 Profilometry

In Chapter 2, an overview was given of the prominent profilometric techniques along with their lateral resolution and application restrictions. Based on this information, it is possible to make a selection of the profilometers that are most suitable for the characterisation of the filter

cake surface. The filter cake should be characterised at micrometre scale, and techniques such as AFM, SEM, STM are mostly used in the lower regions of the microscale and nanoscale. Although a high resolution does not impose a direct problem, this implies a low surface covering capacity and a high price tag, making these profilometers inappropriate for the task at hand. The contact-based modus operandi of stylus profilometry can disturb the surface of the soft filter cake and give rise to faulty measurements. Furthermore, white light axial chromatism provides direct measurements of the distance, in contrast to the interferometry-based techniques where the distance is derived from other measured quantities. Hence, it seems that white light axial chromatism is the most suitable technique for profiling filter cake.

# CHAPTER 7

## Conclusion

Aiming at disclosing the mechanisms of filter cake formation, the model framework established by Ghijs (2014) was successfully extended. The representation of multidisperse feed flows was implemented, enabling a realistic simulation of MBR feed flows characterised by a PSD. Progression was made towards the formation of realistic filter cake structures by transitioning to a three-dimensional model. The implementation of a new filter cake attachment algorithm and new sampling procedures induced an enhanced accuracy and computational efficiency. Furthermore, the model implementation was parallelised, in order to speed-up the calculations and a post-processing tool was developed for a user-friendly analysis of the simulation results. The simulations of the extended model yielded interesting results and several conclusions can be formulated.

First of all, an experimental microfiltration unit for the calibration and validation of the model was designed by means of CFD. The unit presented a perfect laminar flow regime without dead volumes or recirculation streams and enables a simplified representation of the filtration unit, lowering the computational demand of the model. The CFD simulations indicated that in order to obtain such a flow regime, a gradual transition from the inlet to the membrane compartment is imperative.

Next, a qualitative validation showed that the model was able to reproduce the radial migration of non-buoyant particles in a Poiseuille flow, governed by the Segré-Silberberg effect. The theoretically and experimentally acknowledged dependency of the radial migration magnitude on the Reynolds and particle Reynolds number was successfully reproduced by the model. However, the occurrence of an equilibrium position at approximately 60 % of the distance from the center axis to the wall was not observed. This is most likely due to the absence of the wall-induced lift force in the force balance. Furthermore, the effect of the shear gradient-induced lift force should also be investigated in order to determine its relevance for filter cake formation. Through the Segré-Silberberg effect, a spatial segregation of the sus-

pended solids was demonstrated; bigger particles are more influenced by the inertial lift force and migrate faster towards the walls of the tube.

Lastly, a scenario analysis was performed and the results indicated a large effect of polydispersity on the fouling rate and filter cake porosity. Multidisperse feed flows result in a faster filter cake build up and less porous filter cakes than monodisperse feed flows. The need to implement a particle rolling algorithm was concluded due to the formation of unrealistically narrow and high filter cake piles. Additionally, the adhesion equation should be calibrated or replaced with a force balance on the particles attached to filter cake/membrane and a bidirectional coupling between the two model layers should be implemented in order to simulate the increased filtration resistance due to membrane fouling, and predict a flux decline or TMP increase for constant pressure or constant flux membrane filtration systems, respectively.

To conclude, the spatio-temporal model was extended and a considerable progress was made towards realistic filter cake formation simulations. This research has yielded several new insights in the underlying mechanisms of membrane fouling and indicated the importance of the lift force induced migration of suspended solids in tubular membranes as well as the impact of polydispersity.

# Bibliography

- Bender, E. A. (2000). *An Introduction to Mathematical Modeling*. John Wiley & Sons, New York, USA.
- Binnig, G. and Rohrer, H. (1982). Scanning tunneling microscopy. *Surface Science*, 126(126):236–244.
- Broeckmann, A., Busch, J., Wintgens, T., and Marquardt, W. (2006). Modeling of pore blocking and cake layer formation in membrane filtration for wastewater treatment. *Desalination*, 189(1-3):97–109.
- Cao, T. A., Van De Staey, G., and Smets, I. Y. (2015). Integrating activated sludge floc size information in MBR fouling modeling. *Water Science & Technology*, 71(7):1073–1080.
- Catto, C. J. D. and Smith, K. C. A. (1973). Resolution limits in the surface scanning electron microscope. *Journal of Microscopy*, 98(3):417–435.
- Cha, S., Lin, P. C., Zhu, L., Sun, P. C., and Fainman, Y. (2000). Nontranslational three-dimensional profilometry by chromatic confocal microscopy with dynamically configurable micromirror scanning. *Applied optics*, 39(16):2605–2613.
- Charcosset, C. (2014). Combining membrane processes with renewable energy technologies: perspectives on membrane desalination, biofuels and biogas production, and microbial fuel cells. In *Membranes for Clean and Renewable Power Applications*, pages 44–62. Elsevier.
- Cheryan, M. and Rajagopalan, N. (1998). Membrane processing of oily streams. Wastewater treatment and waste reduction. *Journal of Membrane Science*, 151(1):13–28.
- Cimini, A., Marconi, O., and Moresi, M. (2013). Rough beer clarification by crossflow microfiltration in combination with enzymatic and/or centrifugal pretreatments. *Chemical Engineering Transactions*, 32(2013):1729–1734.
- Conroy, M. and Armstrong, J. (2005). A comparison of surface metrology techniques. *Journal of Physics: Conference Series*, 13(2005):458–465.

- Cross, M., Douglas, W. H., and Fields, R. P. (1985). Optimal design methodology for composite materials with particulate fillers. *Powder Technology*, 43(1985):27–36.
- Dalmau, M., Atanasova, N., Gabarrón, S., Rodriguez-Roda, I., and Comas, J. (2015). Comparison of a deterministic and a data driven model to describe MBR fouling. *Chemical Engineering Journal*, 260(2015):300–308.
- Desmond, K. W. and Weeks, E. R. (2014). Influence of particle size distribution on random close packing of spheres. *Physical Review E*, 90(2):022204.
- Di Carlo, D., Irimia, D., Tompkins, R. G., and Toner, M. (2007). Continuous inertial focusing, ordering, and separation of particles in microchannels. *Proceedings of the National Academy of Sciences of the United States of America*, 104(48):18892–7.
- Drews, A., Arellano-Garcia, H., Schöneberger, J., Schaller, J., Wozny, G., and Kraume, M. (2009). Model-based recognition of fouling mechanisms in membrane bioreactors. *Desalination*, 236(1-3):224–233.
- Dubé, M. A., Tremblay, A. Y., and Liu, J. (2007). Biodiesel production using a membrane reactor. *Bioresource Technology*, 98(3):639–647.
- Faxén, H. (1922). Der Widerstand gegen die Bewegung einer starren Kugel in einer zähen Flüssigkeit, die zwischen zwei parallelen ebenen Wänden eingeschlossen ist. *Annalen der Physik*, 373(10):89–119.
- Fu, F. and Wang, Q. (2011). Removal of heavy metal ions from wastewaters: A review. *Journal of Environmental Management*, 92(3):407–418.
- Ghijs, M. (2014). *Spatio-temporal modeling of filter cake formation in membrane bioreactors*. Master thesis, Ghent university.
- Goldstein, J. I., Newbury, D. E., Echlin, P., Joy, D. C., Lyman, C. E., Lifshin, E., Sawyer, L., and Michael, J. R. (2003). *Scanning Electron Microscopy and X-ray Microanalysis*. Springer US, Boston, MA, third edition.
- Gorthi, S. S. and Rastogi, P. (2010). Fringe projection techniques: Whither we are? *Optics and Lasers in Engineering*, 48(2):133–140.
- Hansma, P. K. and Tersoff, J. (1987). Scanning tunneling microscopy. *Journal of Applied Physics*, 61(2).
- Hariharan, P. (2012). Basics of Interferometry. In *Basics of Interferometry*, page 213. Academic Press, San Diego, USA, first edition.
- Hermansson, M. (1999). The DLVO theory in microbial adhesion. *Colloids and Surfaces B: Biointerfaces*, 14(1-4):105–119.

- Hocken, R., Chakraborty, N., and Brown, C. (2005). Optical Metrology of Surfaces. *CIRP Annals - Manufacturing Technology*, 54(2):169–183.
- Homsy, A., van der Wal, P. D., Doll, W., Schaller, R., Korsatko, S., Ratzer, M., Ellmerer, M., Pieber, T. R., Nicol, A., and de Rooij, N. F. (2012). Development and validation of a low cost blood filtration element separating plasma from undiluted whole blood. *Biomicrofluidics*, 6(1):1–9.
- Hubbard, P. M. (1996). Approximating polyhedra with spheres for time-critical collision detection. *ACM Transactions on Graphics*, 15(3):179–210.
- Judd, S. (2008). The status of membrane bioreactor technology. *Trends in Biotechnology*, 26(2):109–116.
- Judd, S. (2011). *The MBR Book: Principles and Applications of Membrane Bioreactors for Wastewater Treatment*. Elsevier Ltd, Oxford, UK, second edition.
- Kemper, B., Langehanenberg, P., and von Bally, G. (2007). Digital holographic microscopy: a new method for surface analysis and marker-free dynamic life cell imaging. *Optik & Photonik*, 2(2):41–44.
- Khalaf, R. M. F. and Bainbridge, D. R. (1981). Nomarski differential interference contrast studies of murine lymphocytes. *European Journal of Immunology*, 11(10):816–824.
- Khan, S. J., Visvanathan, C., and Jegatheesan, V. (2009). Prediction of membrane fouling in MBR systems using empirically estimated specific cake resistance. *Bioresource Technology*, 100(23):6133–6136.
- Koros, W. J., Ma, Y. H., and Shimidzu, T. (1996). Terminology for membranes and membrane processes (IUPAC Recommendations 1996). *Pure and Applied Chemistry*, 68(7):149–159.
- Leach, R. (2011). *Optical Measurement of Surface Topography*. Springer Berlin Heidelberg, Heidelberg, Berlin, first edition.
- Li, H., Fane, A., Coster, H., and Vigneswaran, S. (1998). Direct observation of particle deposition on the membrane surface during crossflow microfiltration. *Journal of Membrane Science*, 149(1):83–97.
- Li, X. Y. and Wang, X. M. (2006). Modelling of membrane fouling in a submerged membrane bioreactor. *Journal of Membrane Science*, 278(1-2):151–161.
- Lonardo, P., Lucca, D., and De Chiffre, L. (2002). Emerging Trends in Surface Metrology. *CIRP Annals - Manufacturing Technology*, 51(2):701–723.
- Lu, W.-M. and Hwang, K.-J. (1993). Mechanism of cake formation in constant pressure filtrations. *Separations Technology*, 3(3):122–132.

- Luque, S., Gómez, D., and Álvarez, J. R. (2008). Industrial Applications of Porous Ceramic Membranes (PressureDriven Processes). *Membrane Science and Technology*, 13(7):177–216.
- Lyklema, J. (1968). Principles of the stability of lyophobic colloidal dispersions in non-aqueous media. *Advances in Colloid and Interface Science*, 2(2):67–114.
- Maere, T., Villez, K., Marsili-Libelli, S., Naessens, W., and Nopens, I. (2012). Membrane bioreactor fouling behaviour assessment through principal component analysis and fuzzy clustering. *Water Research*, 46(18):6132–6142.
- Matas, J. P., Morris, J. F., and Guazzelli, E. (2004). Lateral forces on a sphere. *Oil and Gas Science and Technology*, 59(1):59–70.
- MathWorks (2016). MATLAB web page. <http://nl.mathworks.com/products/matlab/>. Accessed: 20-04-2016.
- Maxey, M. R. and Riley, J. J. (1983). Equation of motion for a small rigid sphere in a nonuniform flow. *Physics of Fluids*, 26(1983):883.
- Meng, F., Zhang, H., Yang, F., Zhang, S., Li, Y., and Zhang, X. (2006). Identification of activated sludge properties affecting membrane fouling in submerged membrane bioreactors. *Separation and Purification Technology*, 51(1):95–103.
- Mirbagheri, S. A., Bagheri, M., Bagheri, Z., and Kamarkhani, A. M. (2015). Evaluation and prediction of membrane fouling in a submerged membrane bioreactor with simultaneous upward and downward aeration using artificial neural network-genetic algorithm. *Process Safety and Environmental Protection*, 96:111–124.
- Mohammadi, T., Madaeni, S. S., and Moghadam, M. K. (2003). Investigation of membrane fouling. *Desalination*, 153:155–160.
- Naessens, W., Maere, T., and Nopens, I. (2012). Critical review of membrane bioreactor models - Part 1: Biokinetic and filtration models. *Bioresource Technology*, 122:95–106.
- Nanovea (2015). Chromatic confocal profilometers, technical sheet. <http://nanovea.com/wp-content/themes/wp-nanovea/brochures/profilers.pdf>. Accessed: 13-02-2016.
- Open-Cascade (2016). SALOME web page. <http://www.salome-platform.org/>. Accessed: 20-04-2016.
- OpenFOAM-Foundation (2016). OpenFOAM web page. <http://openfoam.com/>. Accessed: 20-04-2016.
- Owen, G., Bandi, M., and Howell, J. A. (1995). Economic assessment of membrane processes for water and waste water treatment. 102:77–91.

- Patankar, S. (1980). *Numerical Heat Transfer and Fluid Flow*. Hemisphere Publishing Corporation, first edition.
- Pawley, J. B. (1995). *Handbook of Biological Confocal Microscopy*. Springer Science & Business Media, New York, USA, second edition.
- Picioreanu, C., Vrouwenvelder, J., and van Loosdrecht, M. (2009). Three-dimensional modeling of biofouling and fluid dynamics in feed spacer channels of membrane devices. *Journal of Membrane Science*, 345(1-2):340–354.
- Podoleanu, A. G. (2012). Optical coherence tomography. *Journal of Microscopy*, 247(3):209–219.
- Prasad, N. K. (2010). *Downstream Process Technology: A New Horizon in Biotechnology*. Prentice-Hall Of India Pvt. Limited, New Delhi, India.
- Python-Software-Foundation (2016). Python web page. <https://www.python.org/>. Accessed: 20-04-2016.
- Ranade, V. V. (2002). *Computational flow modeling for chemical reactor engineering*. Academic Press, Massachusetts, USA.
- Reimer, L. (1985). *Scanning Electron Microscopy*. Springer Berlin Heidelberg, Berlin, Heidelberg.
- Roache, P. J. (1997). Quantification of Uncertainty in Computational Fluid Dynamics. *Annual Review of Fluid Mechanics*, 29(1):123–160.
- Rössler Tomas, Hrabovský, M., Jiri, K., and Bartonek, L. (1998). Control of pump blade by moiré topography fringe-shifting method. In *Optical Conference On Wave and Quantum Aspects of Contemporary Optics Proceedings*, pages 161–168.
- Saffman, P. G. (1965). The lift on a small sphere in a slow shear flow. *Journal of Fluid Mechanics*, 22(02):385.
- Scott, K. and Highes, R. (2012). *Industrial Membrane Separation Technology*. Springer Science & Business Media, Dordrecht, Netherlands, first edition.
- Segré, G. and Silberberg, A. (1961). Radial Particle Displacements in Poiseuille Flow of Suspensions. *Nature*, 189(4760):209–210.
- Segré, G. and Silberberg, A. (1962). Behaviour of macroscopic rigid spheres in Poiseuille flow Part 1. Determination of local concentration by statistical analysis of particle passages through crossed light beams. *Journal of Fluid Mechanics*, 14(01):115.

- Shetty, G. R. and Chellam, S. (2003). Predicting membrane fouling during municipal drinking water nanofiltration using artificial neural networks. *Journal of Membrane Science*, 217(1-2):69–86.
- Sohn, H. Y. and Moreland, C. (1968). The effect of particle size distribution on packing density. *The Canadian Journal of Chemical Engineering*, 46(3):162–167.
- Song, J. (1991). Stylus profiling at high resolution and low force. *Applied optics*, 30(1):42–50.
- Stout, K. and Blunt, L. (2000). *Three Dimensional Surface Topography*. Elsevier.
- Su, X. and Chen, W. (2001). Fourier transform profilometry: A review. *Optics and Lasers in Engineering*, 35(5):263–284.
- Tamime, A. Y. (2012). *Membrane Processing: Dairy and Beverage Applications*. John Wiley & Sons, Chichester, UK, first edition.
- Taylor, J. B., Carrano, A. L., and Kandlikar, S. G. (2006). Characterization of the effect of surface roughness and texture on fluid flowpast, present, and future. *International Journal of Thermal Sciences*, 45(10):962–968.
- Tu, J. V. (1996). Advantages and disadvantages of using artificial neural networks versus logistic regression for predicting medical outcomes. *Journal of Clinical Epidemiology*, 49(11):1225–1231.
- Ulbricht, M., Ansorge, W., Danielzik, I., König, M., and Schuster, O. (2009). Fouling in microfiltration of wine: The influence of the membrane polymer on adsorption of polyphenols and polysaccharides. *Separation and Purification Technology*, 68(3):335–342.
- Van Oss, C. J. (1989). Energetics of cell-cell and cell-biopolymer interactions. *Cell Biophysics*, 14(1):1–16.
- Versteeg, H. and Malalasekera, W. (1995). *An Introduction to Computational Fluid Dynamics - The Finite Volume Method*. Longman Scientific & technical, London, UK, first edition.
- Vrouwenvelder, J. S., Picioreanu, C., Kruithof, J. C., and van Loosdrecht, M. C. M. (2010). Biofouling in spiral wound membrane systems: Three-dimensional CFD model based evaluation of experimental data. *Journal of Membrane Science*, 346(1):71–85.
- Whitehouse, D. (1999). Surface metrology. *Computer Standards & Interfaces*, 21(2):185.
- Wintgens, T., Rosen, J., Melin, T., Brepols, C., Drensla, K., and Engelhardt, N. (2003). Modelling of a membrane bioreactor system for municipal wastewater treatment. *Journal of Membrane Science*, 216(1-2):55–65.

Wörner, M. (2003). A Compact Introduction to the Numerical Modeling of Multiphase Flows. Technical report, Karlsruhe, Germany.

Yoon, S., Lee, C., Kim, K., and Fane, A. G. (1999). Three-dimensional simulation of the deposition of multi-dispersed charged particles and prediction of resulting flux during cross-flow microfiltration. *Journal of Membrane Science*, 161:7–20.

Zeng, L., Balachandar, S., and Fischer, P. (2005). Wall-induced forces on a rigid sphere at finite Reynolds number. *Journal of Fluid Mechanics*, 536:1–25.

Zhang, S. (2010). Recent progresses on real-time 3D shape measurement using digital fringe projection techniques. *Optics and Lasers in Engineering*, 48(2):149–158.

Zikanov, O. (2010). *Essential Computational Fluid Dynamics*. John Wiley & Sons, Hoboken, USA, first edition.



# APPENDIX A

## Technical drawing microfilter

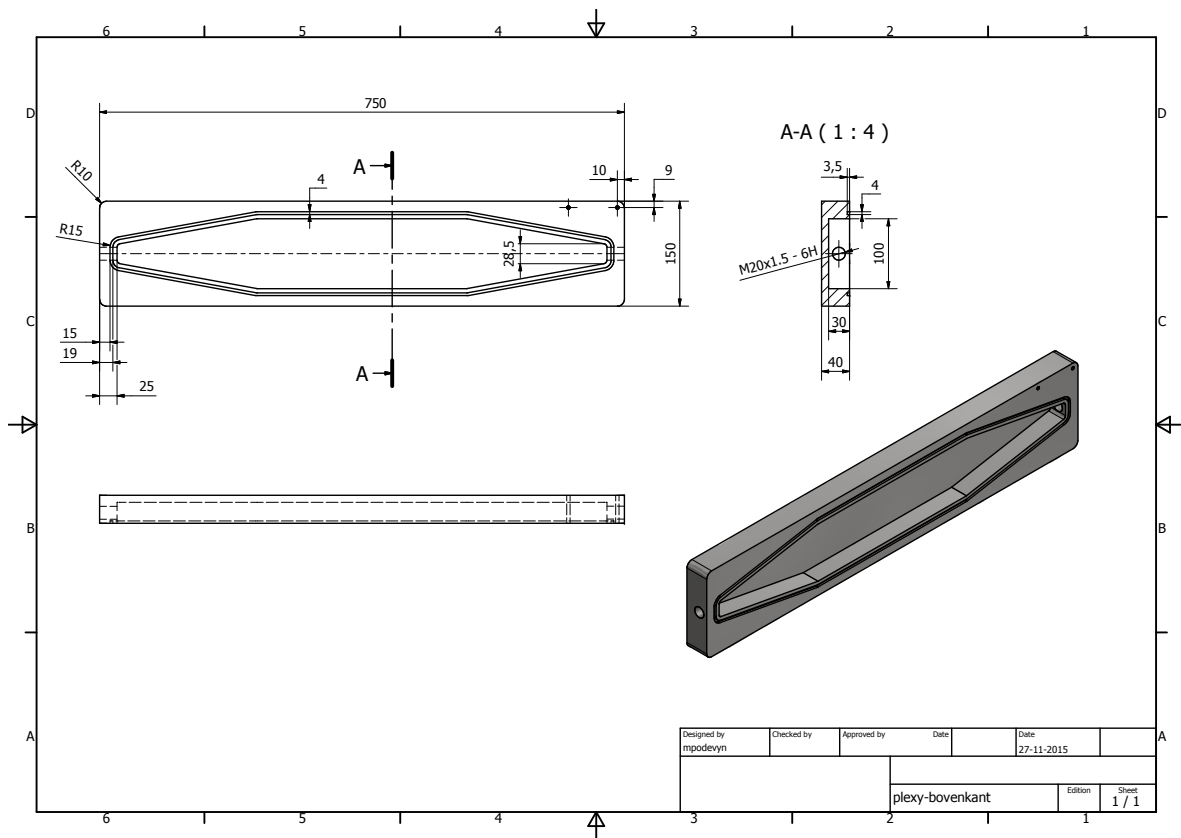


**Figure A.1:** Technical drawing of the microfiltration device